Supplementary Information

Double stress of waterlogging and drought drives forest-savanna coexistence

Caio R. C. Mattos, Marina Hirota, Rafael S. Oliveira, Bernardo M. Flores, Gonzalo Miguez-Macho, Yadu Pokhrel, Ying Fan

This document contains:

MATERIAL AND METHODS

1. Study area

Our study area is tropical South America, defined between 35°S-15°N as in previous studies (1–4) which examined forest and savanna distribution over the continent. To avoid temperature effects on vegetation introduced by high altitude, we restrict our analyses to areas below 1,200 m of elevation following Staver et al. (2011)(5), using the HydroSHEDS digital elevation model at the 1 km resolution.

To explore the regional-scale patterns of waterlogging and vegetation, we zoom in on six insets in the order of decreasing annual precipitation and increasing seasonality: the Pastaza-Marañón Foreland Basin (PMFB), Peru; Marajó Island, Brazil; Llanos de Orinoco, Venezuela and Colombia; Llanos de Moxos, Bolívia; Bananal Island, Brazil; and the Brazil portion of the Pantanal floodplains. Limits for the PMFB were obtained from the literature (6) ,for Marajó Island from the Brazilian Instituto Chico Mendes de Conservação da Biodiversidade (https://www.gov.br/icmbio/pt-br/servicos/geoprocessamento/mapa-tematico-e-dados-geoestatisticos-das-unidades-de-conservacao-federais), for Llanos de Orinoco from the World Wildlife Fund (WWF) Terrestrial Ecoregions of the World(7) (https://www.worldwildlife.org/publications/terrestrial-ecoregions-of-the-world), and for Llanos de Moxos from the Conservation Biology Institute (https://databasin.org/datasets/1520177b6b09402a891a5bc27dd0591a/). For Bananal Island we delimited the area using satellite imagery and for the Brazilian Pantanal from the Terrabrasilis platform maintained by the Brazilian National Institute for Space Research (INPE) (http://terrabrasilis.dpi.inpe.br/en/download-2/).

2. Tree cover and land use data

We use tree cover data from the MODIS MOD44B v6 Vegetation Continuous Fields (VCF) product (8), at 250 m resolution for the year 2017. All pixels with tree cover equal to or greater than 60% are classified as forest, while those below are classified as savanna. Our threshold follows previous studies (1, 2, 4) in the tropics reporting the distribution of forests (high tree cover) and savannas (low tree cover). Although some studies have questioned whether the bimodality is an artifact derived from biases in remote sensing

data(9, 10), others have shown that the signal is much stronger than possible biases (11) and independent analyses using other remote sensing datasets have confirmed these results (12), adding confidence to the use of the MODIS VCF product to distinguish between high and low tree cover.

We carefully exclude all pixels influenced by anthropogenic land-use change that could artificially lower tree cover. We combine the land cover MAPBIOMAS Version 6 product (13) for Brazil with the MAPBIOMAS Amazonia Version 3 at 30 m resolution for the year 2017. Because these products do not cover our entire study area, we use the Copernicus Global Land Cover (14) product outside Brazil, which is at 100 m resolution also for the year of 2017. Because the MAPBIOMAS product has higher accuracy, we keep it where available and use the Copernicus product elsewhere. We also exclude pixels classified as non-natural or open water. Description of each land cover class excluded are given in Table S1.

Table S1 – List and description of human-influenced land cover classes excluded from our analyses from the Copernicus Global Land Cover, MAPBIOMAS Brazil and Amazonia products

Code	**Copernicus**	**MAPBIOMAS Brazil**	**MAPBIOMAS Amazonia**
9	-	Forest plantation	-
14	-	Farming	Farming
15	-	Pasture	-
18	-	Agriculture	-
19	-	Temporary crop	-
20	-	Sugar cane crop	-
21	-	Mosaic of uses (anthropogenic)	-
22	-	Non-vegetated areas	Non-vegetated areas
24	-	Urban area	Urban area
25	-	Other non-vegetated areas	Other non-vegetated areas
26	-	Water	Water
27	-	Not observed	Not observed
30	-	Mining	Mining
31	-	Aquaculture	-

33	-	River, Lake, Ocean	River, Lake, Ocean
34	-	-	Glacier
36	-	Perennial crop	-
39	-	Soybean crop	-
40	Cultivated and managed vegetation/agriculture (cropland)	Rice crop	-
41	-	Other temporary crops	-
46	-	Coffee crop	-
47	-	Citrus crop	-
48	-	Other perennial crops	-
50	Urban / built up	-	-
80	Permanent water bodies	-	-
200	Open sea	-	-

3. Potential analysis

We use the potential analysis method to identify precipitation ranges that support forests, forest-savanna transition zone, and savannas based on probability theories, for the making of Fig 1b and subsequent analyses. The method (15) constructs an empirical stability landscape of tree cover versus mean annual precipitation and has been used extensively in studies concerned with forest-savanna distribution (1, 16). To define the precipitation range in which tree cover shows bistability we use tree cover data at 1 km resolution (see details in "Upscaling" section below) and mean annual precipitation obtained from the ERA5-Land reanalysis monthly precipitation product(17) resampled to 1 km resolution (originally 0.1°; ~10km at the equator) for the 1981-2020 period. The ERA5-Land product has finer horizontal resolution (9km, compared to 31km in ERA5 and 80km in ERA-Interim) and better represents precipitation, soil moisture and river discharge (18). First, we determine the empirical probability distribution of tree cover on a 10^6 sample using a Gaussian kernel estimator (MATLAB function *ksdensity*) with 7% bandwidth and Gaussian weights set as 0.05 times the precipitation range(1). We detect local maxima and minima

numerically and filter out small maxima/minima using a 0.03 threshold(1), and local minima are interpreted as stable states. We define low precipitation as the range where only low tree cover is stable, intermediate precipitation as the bistability range and high precipitation as the range where only high tree cover is dominant (Fig S1).

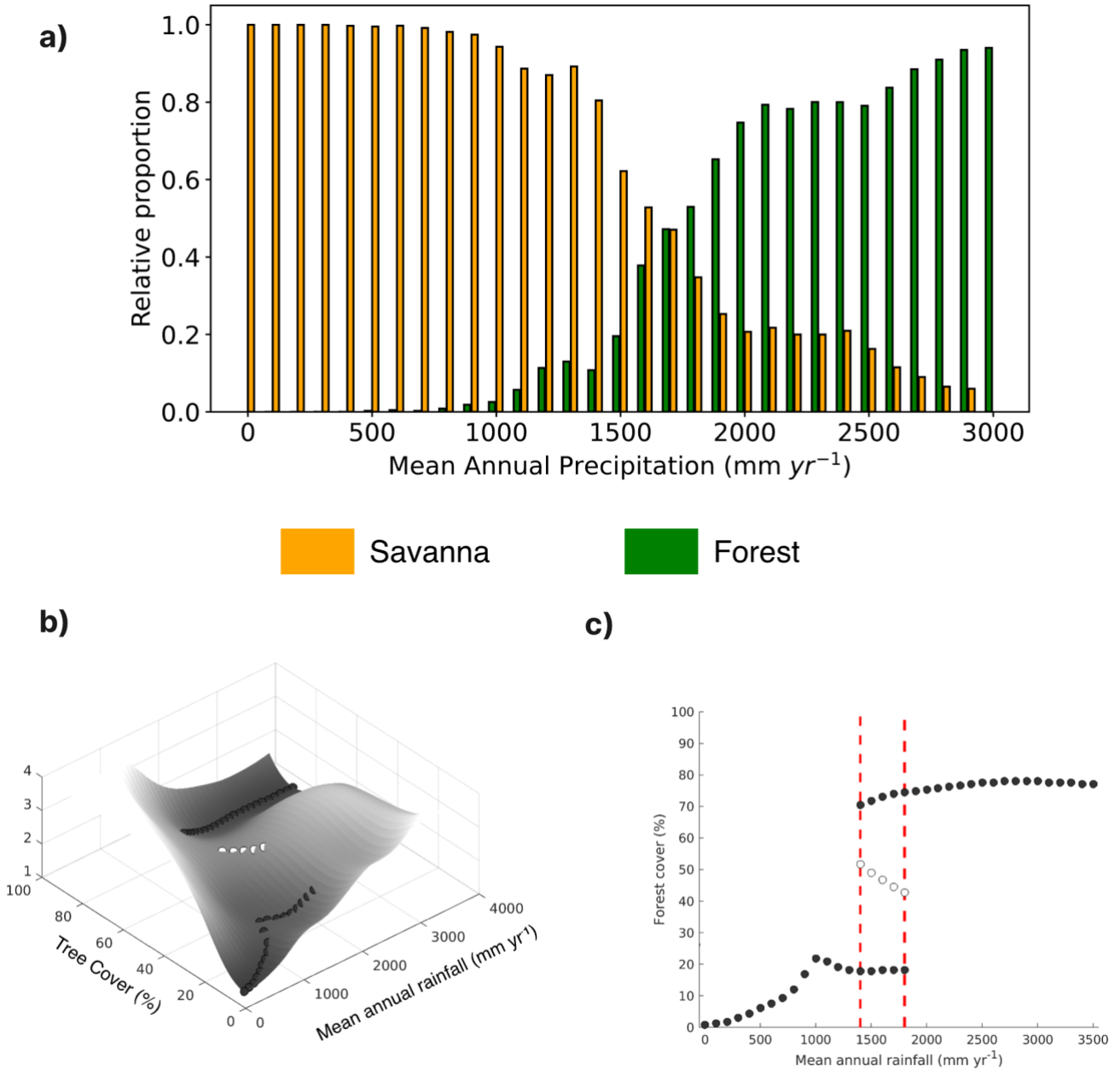

Fig. S1. Potential analysis results for tree cover against mean annual precipitation for tropical South America. (a) Tree cover frequency along a mean annual precipitation (MAP; mm yr^{-1}) gradient, (b)

Three-dimensional stability landscape. Black dots represent valleys and thus stable states, while white dots represent ridges and unstable states. Mean annual rainfall is shown on the x axis, tree cover in the y axis and normalized potential in the z axis (values not shown for clarity) (c) Bifurcation plot, with the red lines representing the calculated bi-stability range of 1400-1800 mm yr^{-1}. In this range, high and low tree cover are considered alternative states.

4. Dynamic hydrological model

Direct observations of water table (WT) depth, the critical hydrologic indicator we use to quantify drought and waterlogging, are sparse over the neotropics, far from representing the WT seasonal change along topographic (hill to valley) and climate (ever-wet to severe dry season) gradients across the vast tropical South America. We thus rely on model simulations that integrate essential water stores and fluxes, forced by observed atmosphere, terrain, and vegetation biomass, to constrain the seasonal WT depth at regular spatial-temporal grids over the continent, that is internally and dynamics consistent with the observable fields.

Our land hydrology model has been described in detail earlier (19–22) and here we briefly describe its basic structure. We represent the South America continent as grid cells of 30-arcsecond (~1 km) to differentiate upland vs. lowland within computational limits, and at hourly steps for 15 years (2003–2018) to resolve event-to-seasonal dynamics. The model has two parts: (i) a fully interactive soil-groundwater-river hydrology forced by atmospheric reanalysis ERA5 (https://www.ecmwf.int/en/forecasts/dataset/ecmwf-reanalysis-v5), observed soil texture and land topography, giving infiltration, soil water profile, WT depth and streamflow and flooding at each hour and grid cell; the porosity and permeability of each column decrease exponentially with depth from top 1m values given in global soil database, the rate of decrease depending on land slope, so that the regolith is shallow on steep slopes and deep in sedimentary basins; vadose zone soil water is calculated with 1D Richards equation, and groundwater below the water table flows from hills to valleys driven by Darcy's law; rivers-floodplains exchange with groundwater freely driven by hydraulic gradients; (ii) soil evaporation and ecosystem transpiration driven by hourly reanalysis atmosphere and daily satellite leaf area index, giving hourly plant water demand to be met by root uptake; (iii) dynamic root water uptake distributed among soil layers using Ohm's law (Fig. S2), so that uptake is higher from wetter (lower

resistance) and shallower (shorter lifting) soil layers. The introduction of dynamic root water uptake, to meet evapotranspiration needs, made the water table deeper globally by directly simulating the effect of vegetation on hydrology (Fig. S3). These processes, driven by observed external forces (climate, terrain), fully interacting with dynamic 2-way exchange among all reservoirs, based on first principles (mass and momentum conservation, potential driven flow such as Darcy's law and Ohm's law), produced a regularly gridded, hourly change of water table depth over 15 years. We saved the monthly water table depth to quantify seasonal drought and waterlogging. Fig. S4 gives the map of annual mean precipitation and water table depth, the latter revealing fine-scaled spatial structure due to topographic relief that drives lateral groundwater flow, absent in the broad-stroked precipitation patterns.

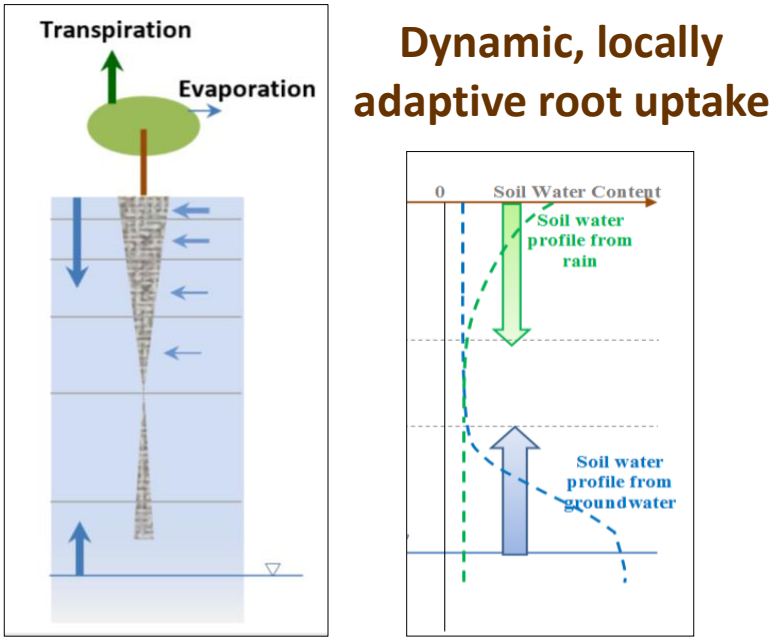

Fig. S2. Schematic representation of the dynamic rooting depth and deep soil water root uptake calculation. (a) Root water uptake from "parallel-connected" soil layers illustrating the distribution of roots and their water extraction. Blue horizontal line with triangle indicates the level of the water table (b) Depiction of soil water potential (blue dashed line) and the ease function (green solid line) profiles, demonstrating their relationship and influence on root water uptake. Solid blue line represents the water table depth. This allows the soil-groundwater hydrology to influence root uptake, and root uptake to influence soil-groundwater hydrology by reducing soil moisture and groundwater recharge.

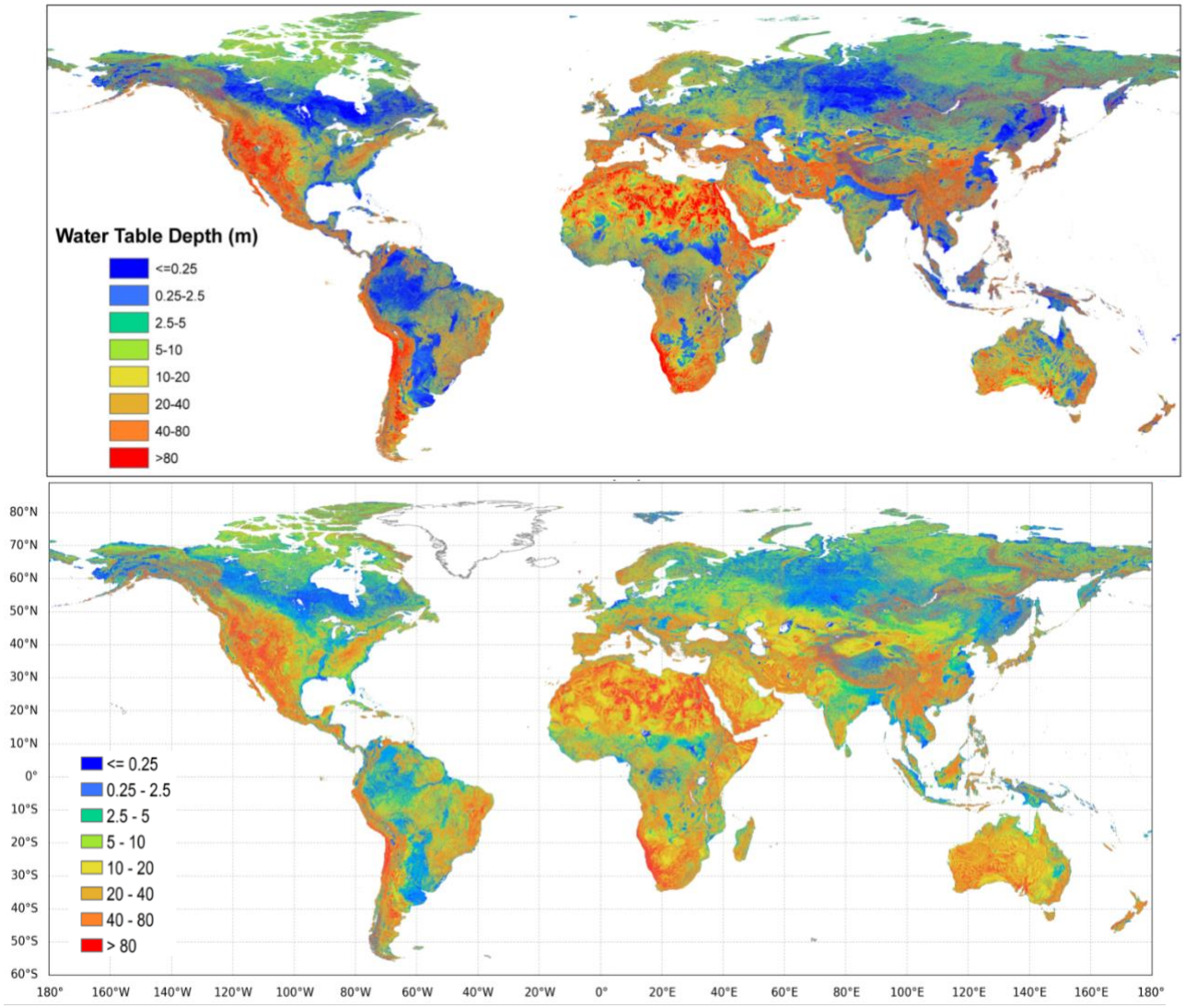

Fig. S3. Comparison of modeled mean water table depth under different root uptake assumptions. (a) Static root uptake scenario based on the non-interactive approach by (23), and (b) Dynamic root uptake scenario incorporating interactive and deep uptake driven by observed leaf area index, atmospheric vapor pressure deficit, and soil moisture profiles determined both by infiltration from the top and capillary rise from the bottom (21). The difference reflects the profound influence of plant water use on land hydrology.

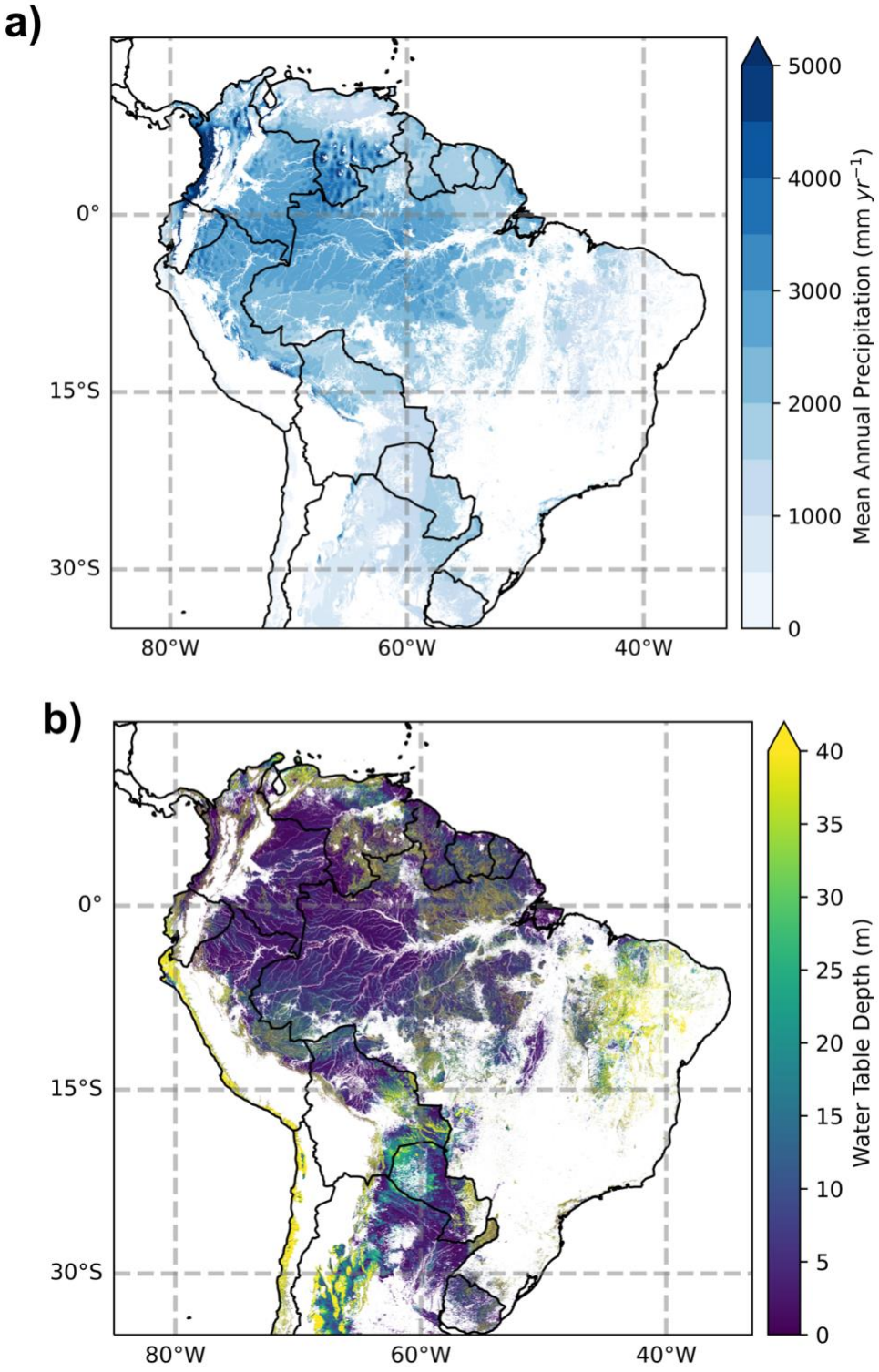

Fig. S4 – Maps for (a) mean annual precipitation (mm yr^{-1}) and (b) mean water table depth (m) for Tropical South America. Note the fine-scaled structure in water table depth under a given climate. White pixels correspond to areas excluded from analyses (e.g., open water, agriculture, high elevations).

We took great care to validate our model using available observations, at multiple scales. In the past 15 years we have validated the model systematically (Tab S2). First, we compared model results against observed daily to monthly soil moisture at multiple depths in N. America (24) and the Amazon (20). Second, we compared our modeled water table depth with 10s of thousands of well observations over N. America (25, 26), S America (20, 27) and 1.6 million well observations over the globe (23). Third, we validated our modeled stream flow against gage observations in N. America (24), the Amazon (19), and globally (21, 22). Fourth, modeled monthly evapotranspiration (ET) is compared with observations at 103 flux-tower sites (21, 22). Fifth, we validated our modeled total terrestrial water storage (TWS), monthly, and integrated vertically over surface water (river and floodplain), soil water (in dynamically deepening or shallowing vadose zone) and groundwater (all water below the water table) against GRACE satellite observations over six large windows in the Amazon (28). Sixth, we validated the capacity of our modeled water table depth in representing waterlogging, or wetland distribution and extent against mapped wetlands in N. America (26) and flooded vs. non-flooded wetlands in S. America (19). In all validations, our model realistically reproduced the observed spatial patterns and seasonal dynamics (timing and amplitude), without calibration of any parameters to match the observations.

Here we show validations for our latest global simulations from which we derive our hydrological data, include comparisons of ET at 103 eddy-covariance flux towers (Fig. S5), river discharge compared to observations at 34 gauges (Fig. S6), and South America comparisons of mean WT at 4885 well observations (Fig. S7) and seasonal WT at 12 sites with time series (Tab S2, Fig. S8), and monthly total water storage change compared to GRACE observations (Fig. S9). Again, without any calibration, the model reproduces the amplitude and timing of seasonal water balance at point scales and across the continent. Discrepancies are due to neglecting anthropogenic activities in the model (irrigation affecting ET, and diversion and reservoir regulation affecting streamflow and water storage).

Table S2. Past comparisons of model output with observations.

Reference	Model output variables and observations used to validate	Model domain	Spatial resolution	Temporal resolution
Fan et al. 2007 (25)	Water table depth at 549,616 well sites	N. America	12.5km	Equilibrium
Miguez-Macho et al. 2007 (24)	Streamflow at 5 gages in Mississippi basin	N. America	12.5km	Daily
	Soil moisture at 19 sites in Illinois	N. America	12.5km	Daily
	Soil moisture at 60 sites in Oklahoma	N. America	12.5km	Bi-weekly
Fan and Miguez-Macho 2010 (27)	Water table depth at 34,351 well sites	S. America	~270m (9")	Equilibrium
Fan and Miguez-Macho 2011 (26)	Wetland distribution and extent	N. America	~270m (9") and ~1km (30")	Equilibrium
Miguez-Macho and Fan 2012a (19)	Streamflow at 10 gages in Amazon	Amazônia	~2km (1')	Daily
	Water table depth at 8 sites reported in the literature	Amazônia	~2km (1')	Daily to monthly
	Surface flooding frequency and extent	Amazônia	~2km (1')	monthly
Miguez-Macho & Fan 2012b (20)	Soil moisture at 7 sites reported in the literature, each site at multiple depths	Amazônia	~2km (1')	Daily to monthly
	Flux tower ET at 6 tower sites	Amazônia	~2km (1')	Monthly
Fan et al. 2013 (23)	Water table depth at 1,603,781 well sites across the globe	Global	~1km (30")	Equilibrium
Pokhrel et al. 2013 (28)	Total terrestrial water storage change observed by GRACE satellites	Amazônia	1 x 1 degree	Monthly

Miguez-Macho and Fan 2021 (22)	Flux-tower ET at 103 tower sites around the globe for a decade (2004-2014)	Global	~1km (30”)	Monthly
	Gage streamflow at 34 gages around the globe for a decade (2004-2014)	Global	~1km (30”)	Monthly

4.1. Comparison of evapotranspiration with flux tower observations

Figure S5a presents the global distribution of eddy-covariance flux towers from the FLUXNET database (https://fluxnet.org/data/fluxnet2015-dataset/). The majority of Amazon data originates from the LBA-ECO CD-32 Flux Tower Network Brazil (https://daac.ornl.gov/LBA/guides/CD32_Brazil_Flux_Network.html) and other published sources. Our study includes 103 sites across 30 countries, with varying periods of overlap with our model: over 6 years in North America and Europe, over 5 years in Australia, and over 1 year in South America, Asia, and Africa, where tower data is limited. Figs. S5b-g display monthly comparisons at these sites, grouped by continent. The vertical axis represents evapotranspiration (ET) in mm/day, while the horizontal axis indicates time (years) in monthly increments. Blue lines depict observed data, and red lines represent our model's results. For comparison purposes, we combined canopy evaporation, soil evaporation, and plant transpiration to calculate total ET, as flux-tower measurements encompass total ET.

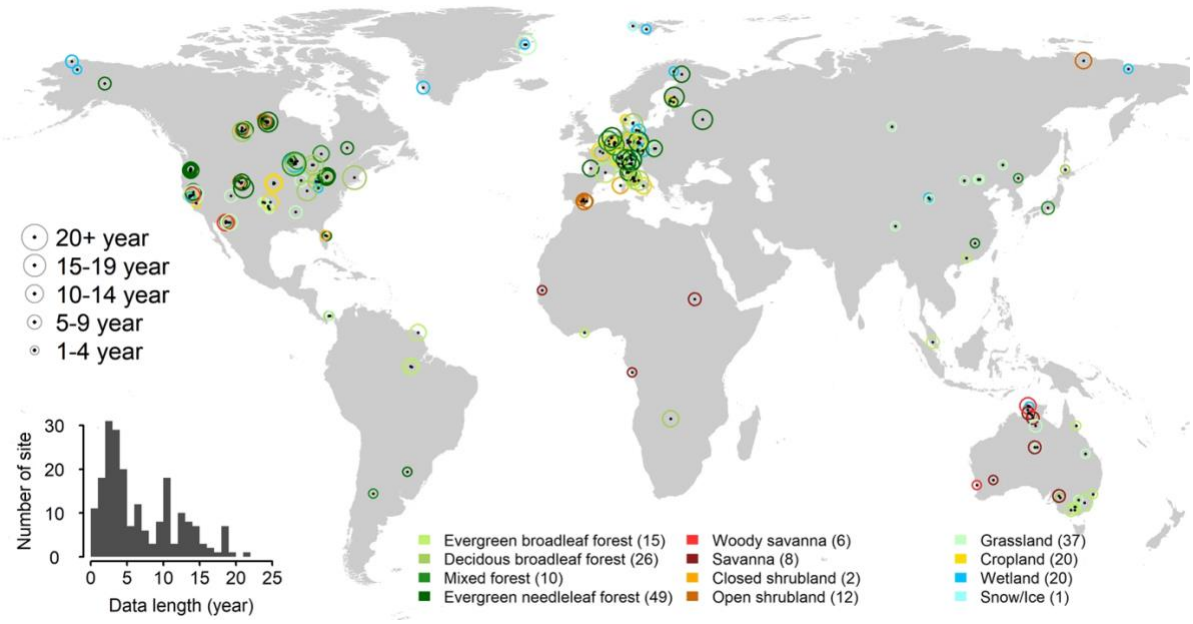

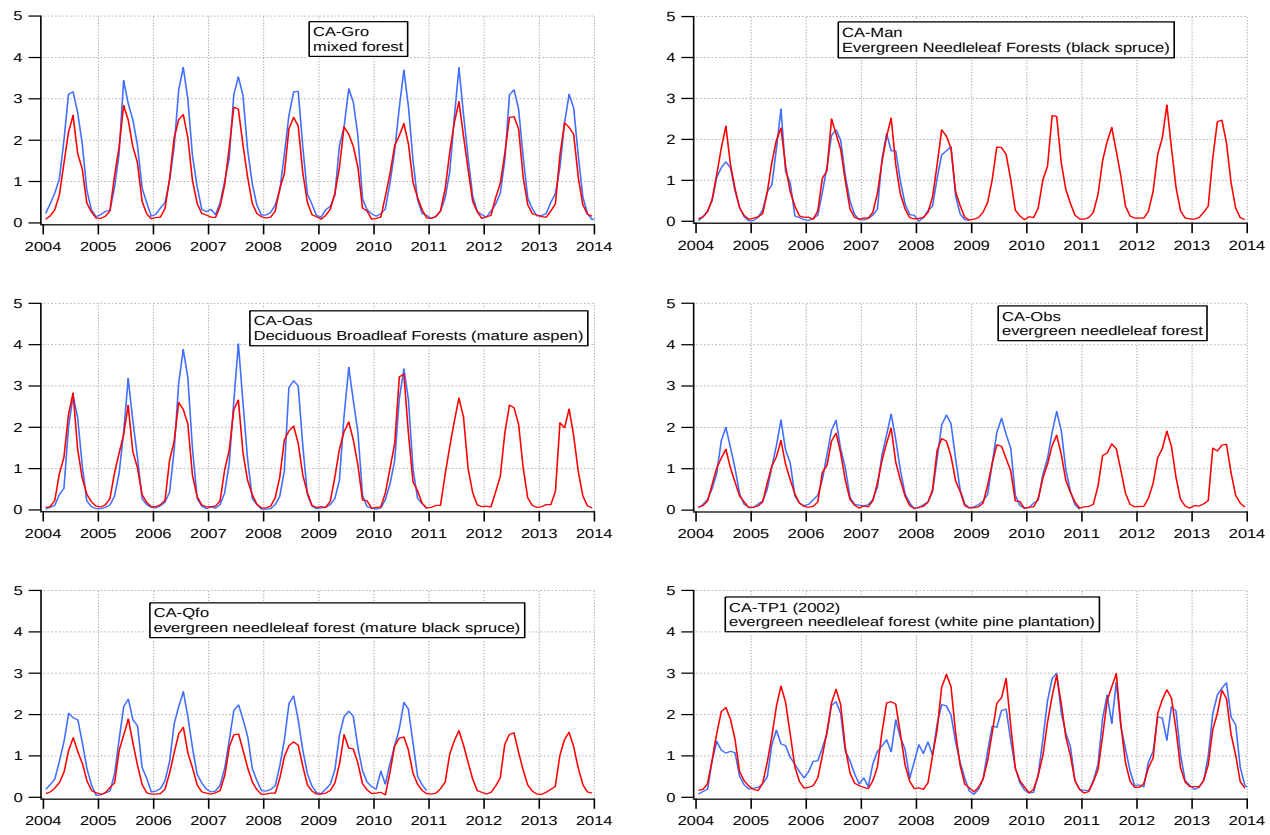

Fig. S5. (a) Location, vegetation type and time series length for flux towers used in our comparison. (b-g) Comparison between observed (blue) and model (red) monthly ET (mm/day) at 103 long-term eddy-flux towers around the globe.

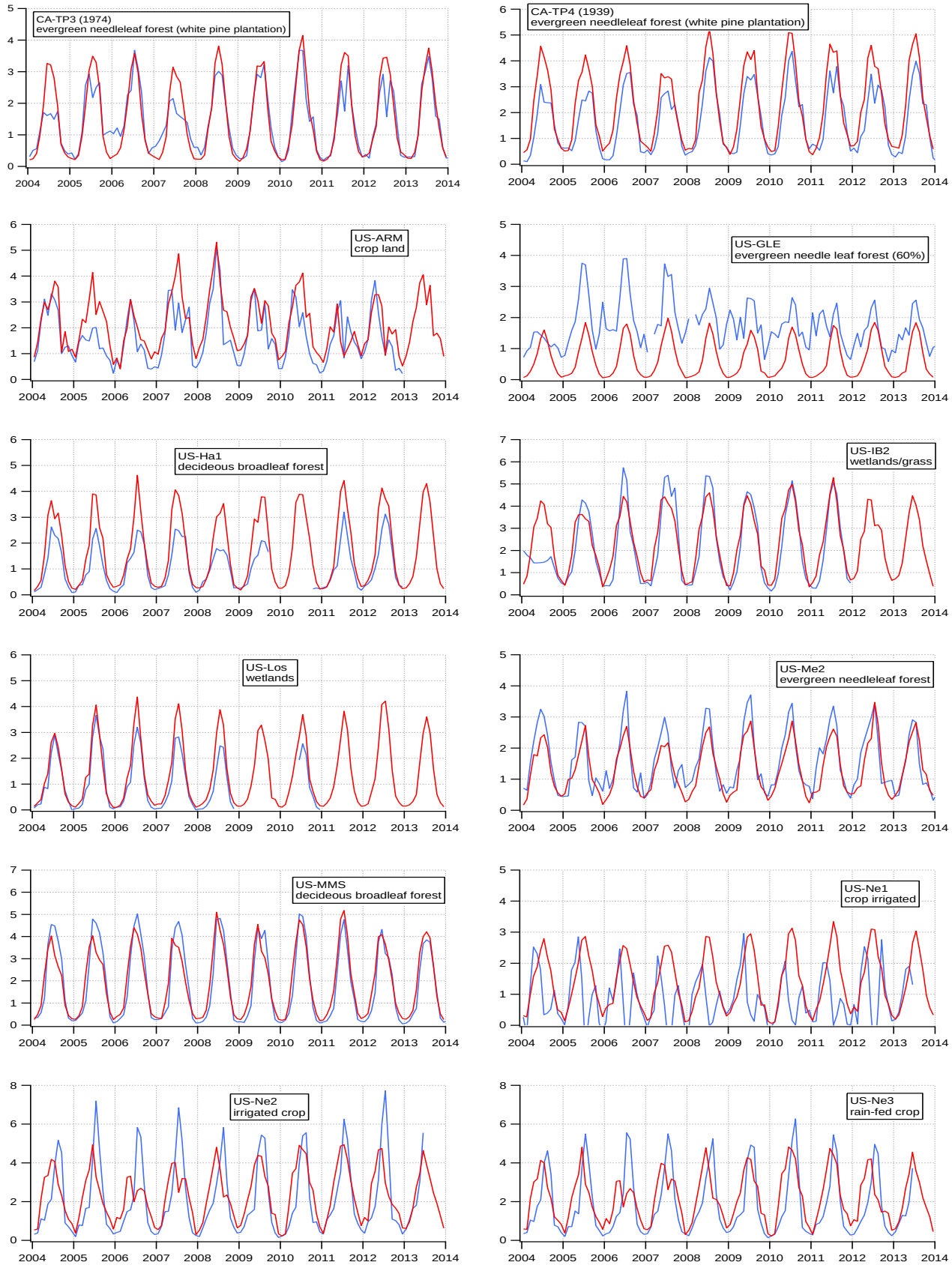

Fig. S5. Continued.

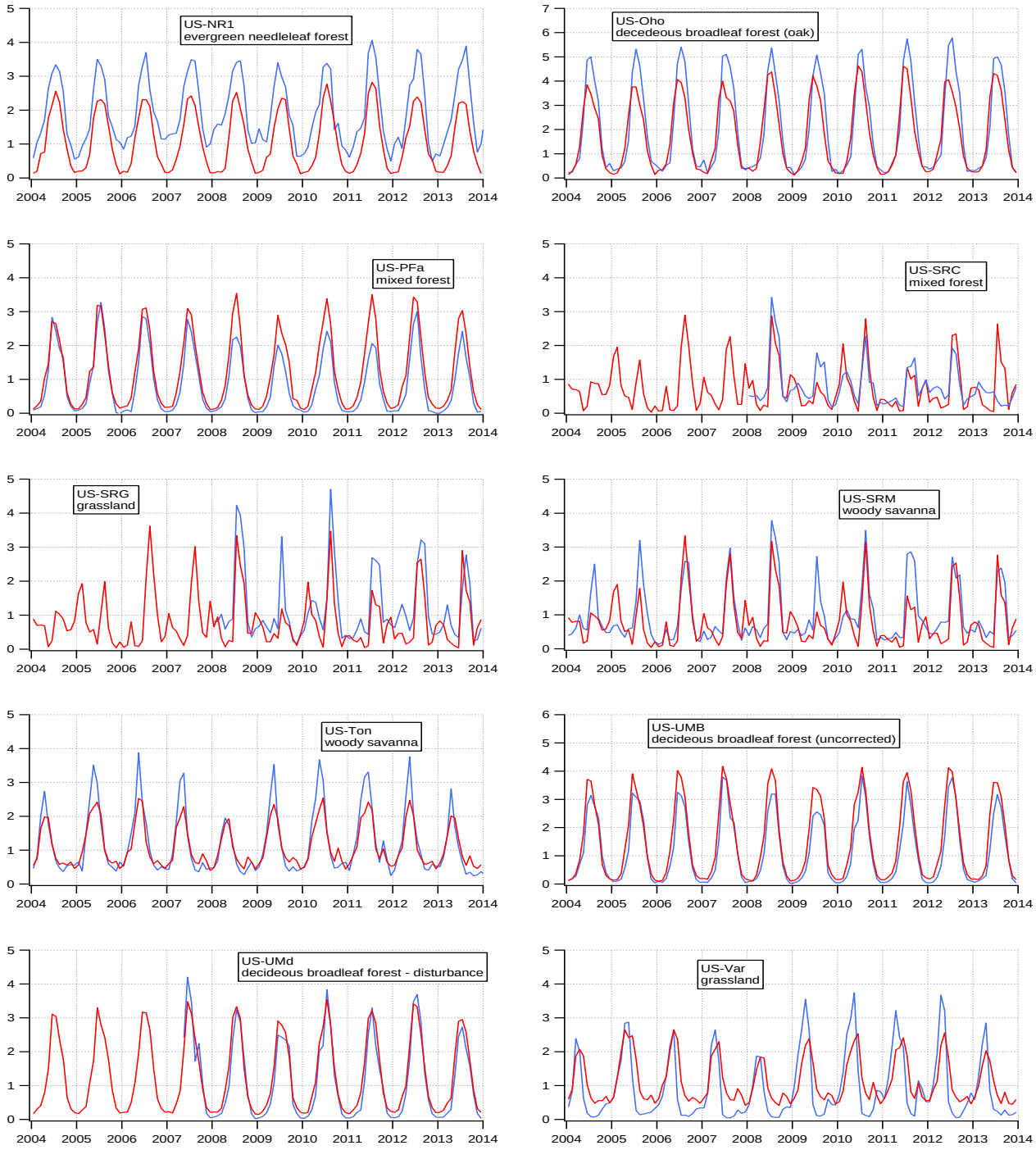

Fig. S5. Continued.

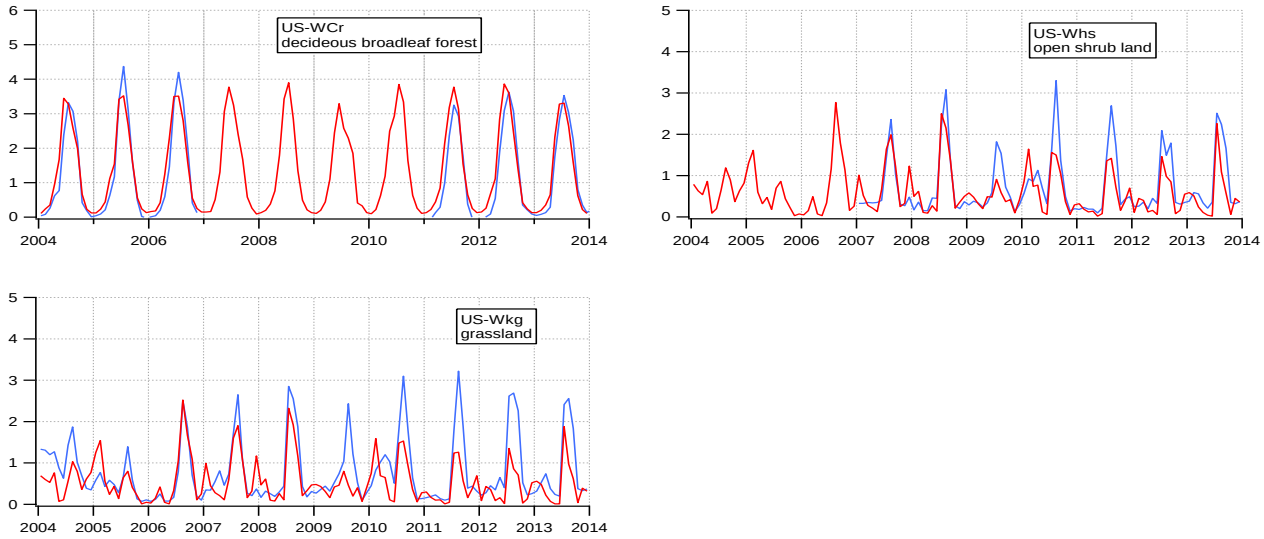

(c) South America (10 sites)

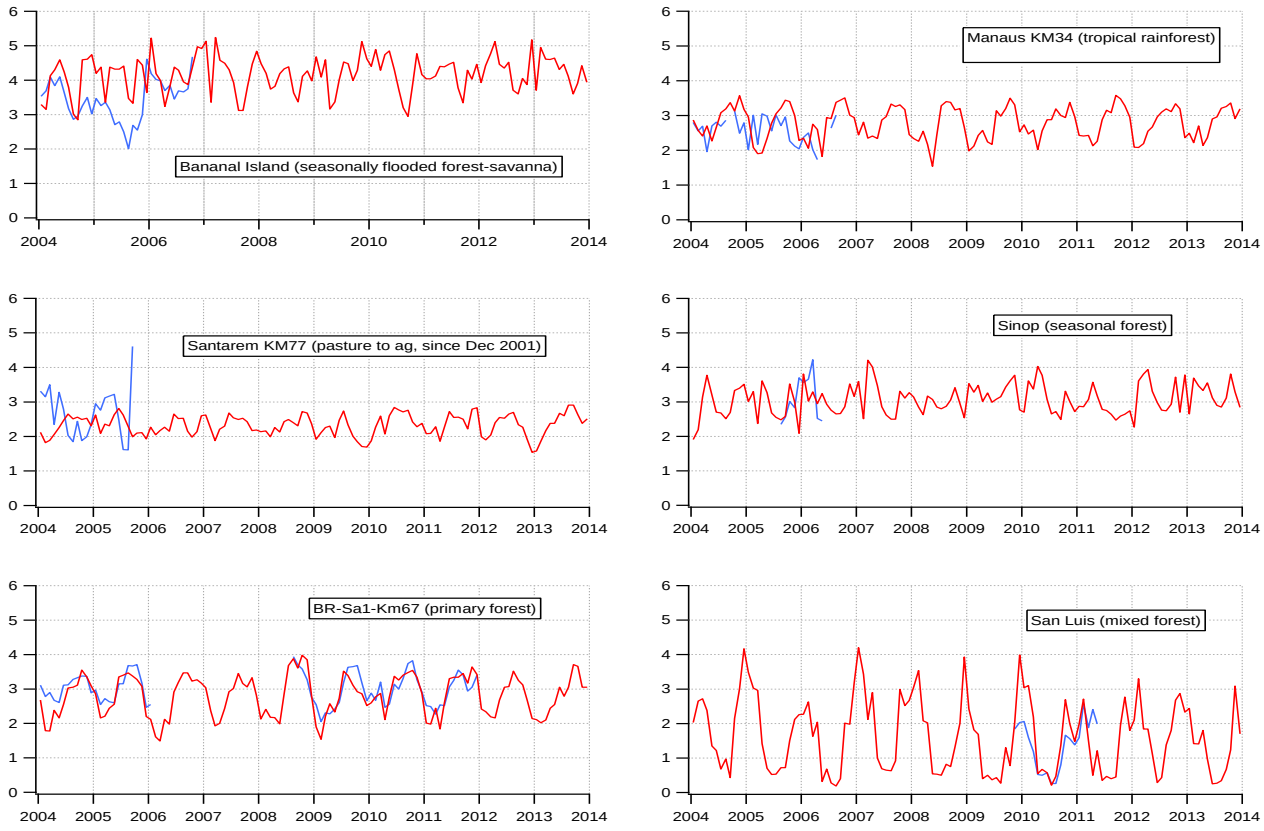

Fig. S5. Continued.

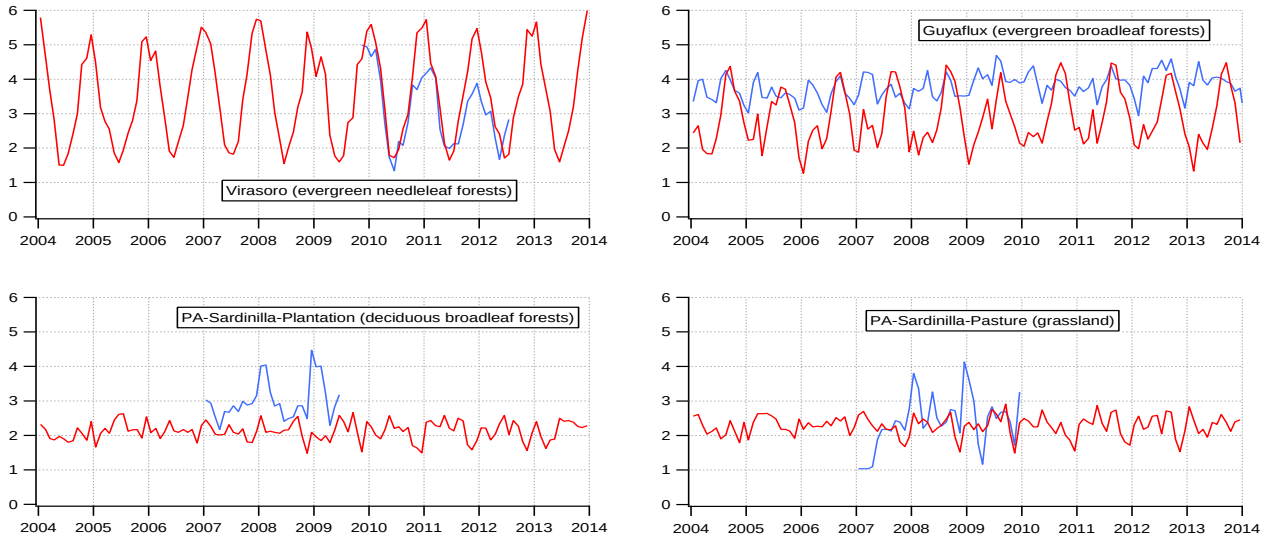

(d) Europe (37 sites)

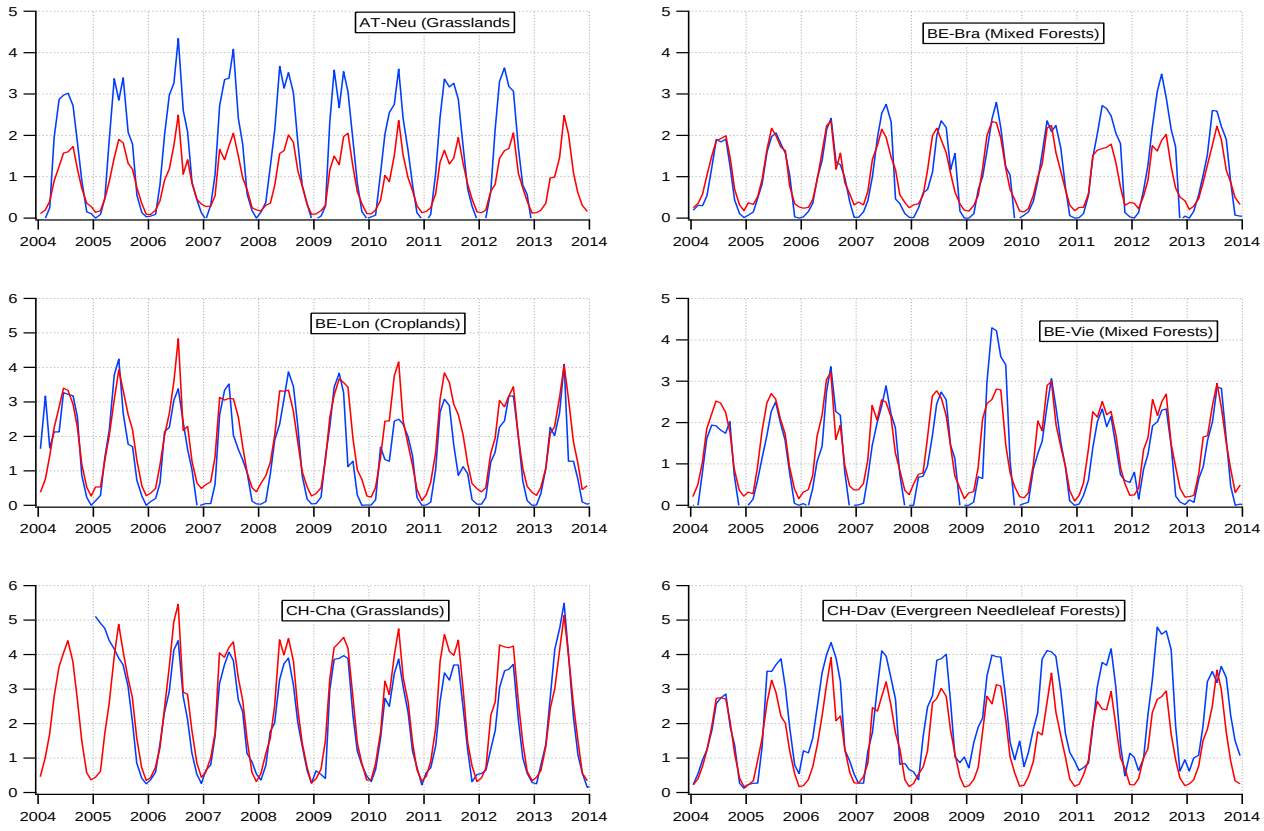

Fig. S5. Continued.

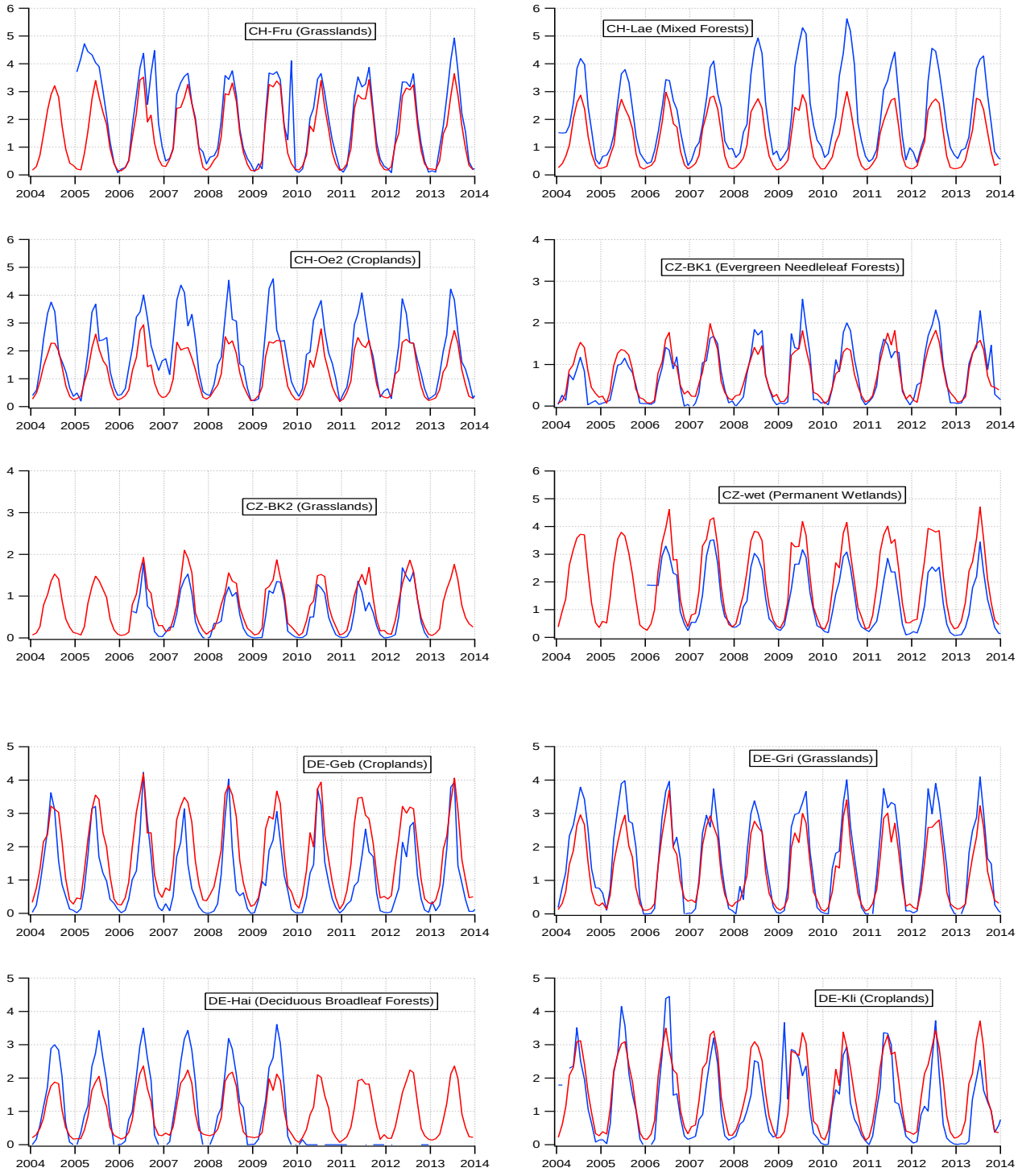

Fig. S5. Continued.

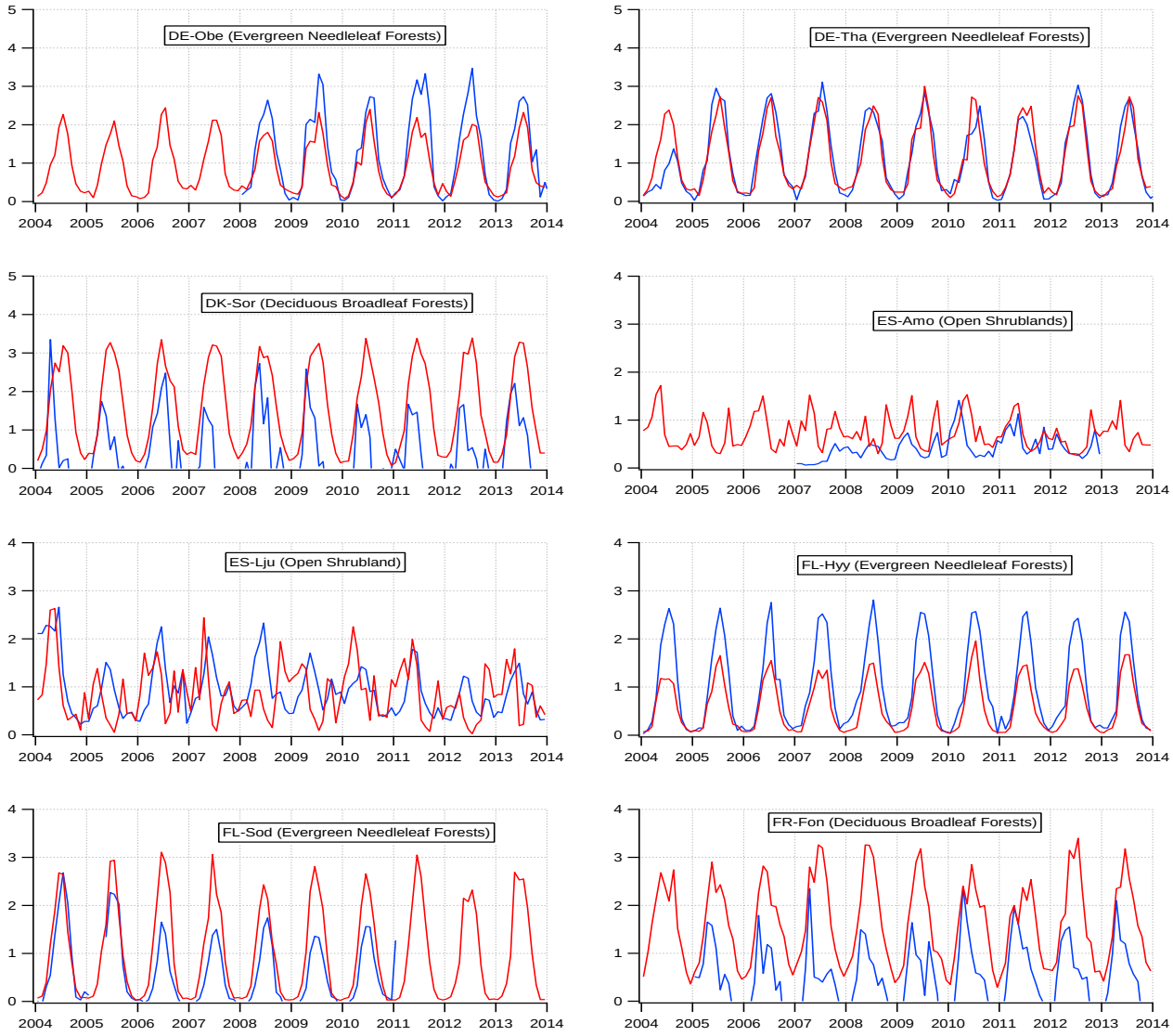

Fig. S5. Continued.

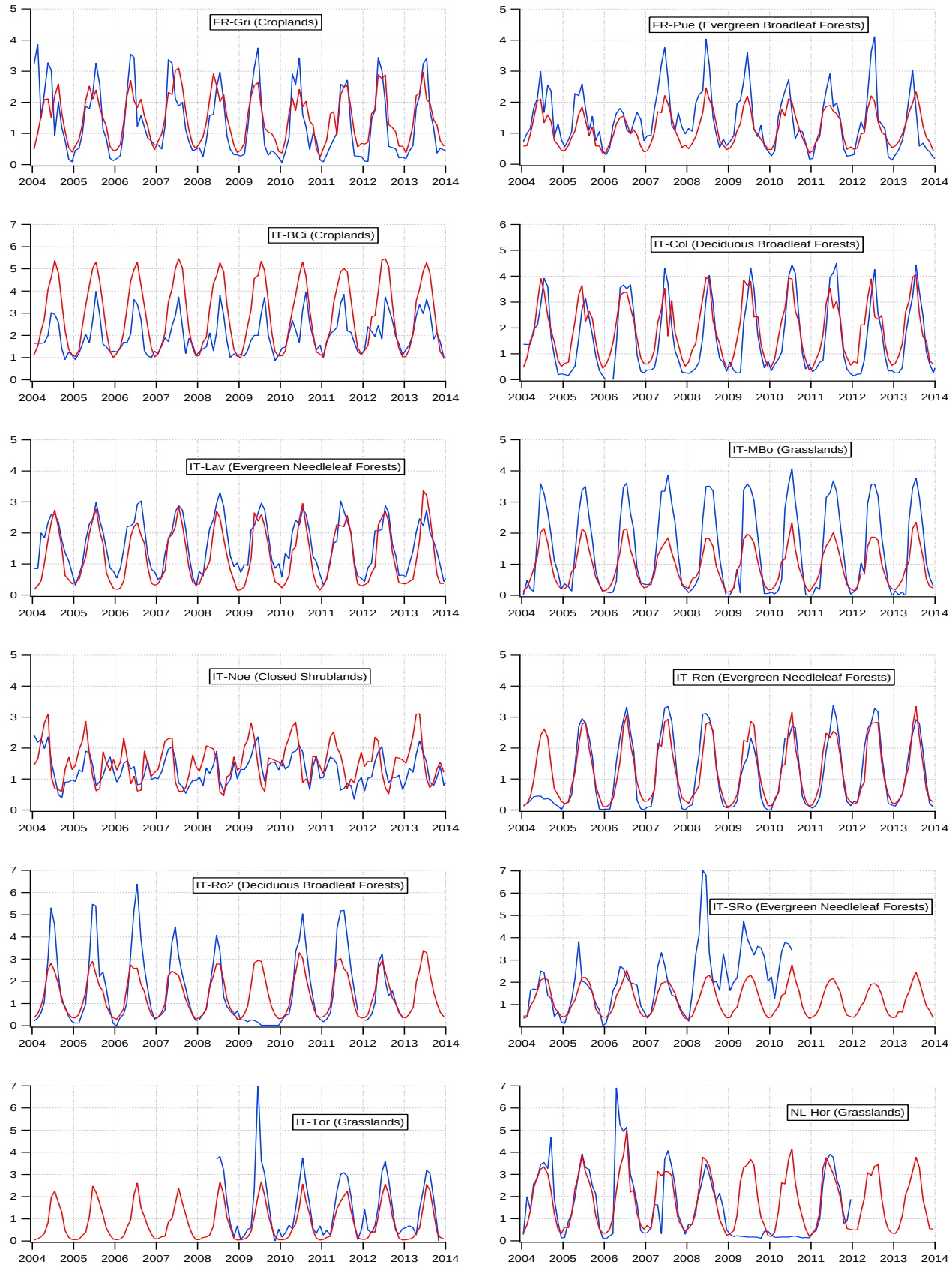

Fig. S5. Continued.

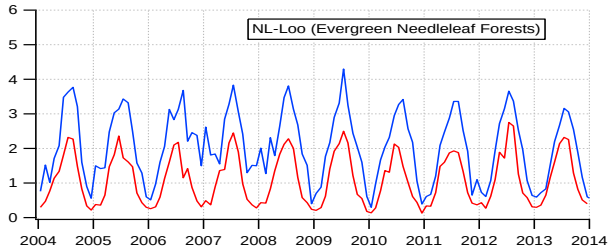

(e) Africa (6 sites)

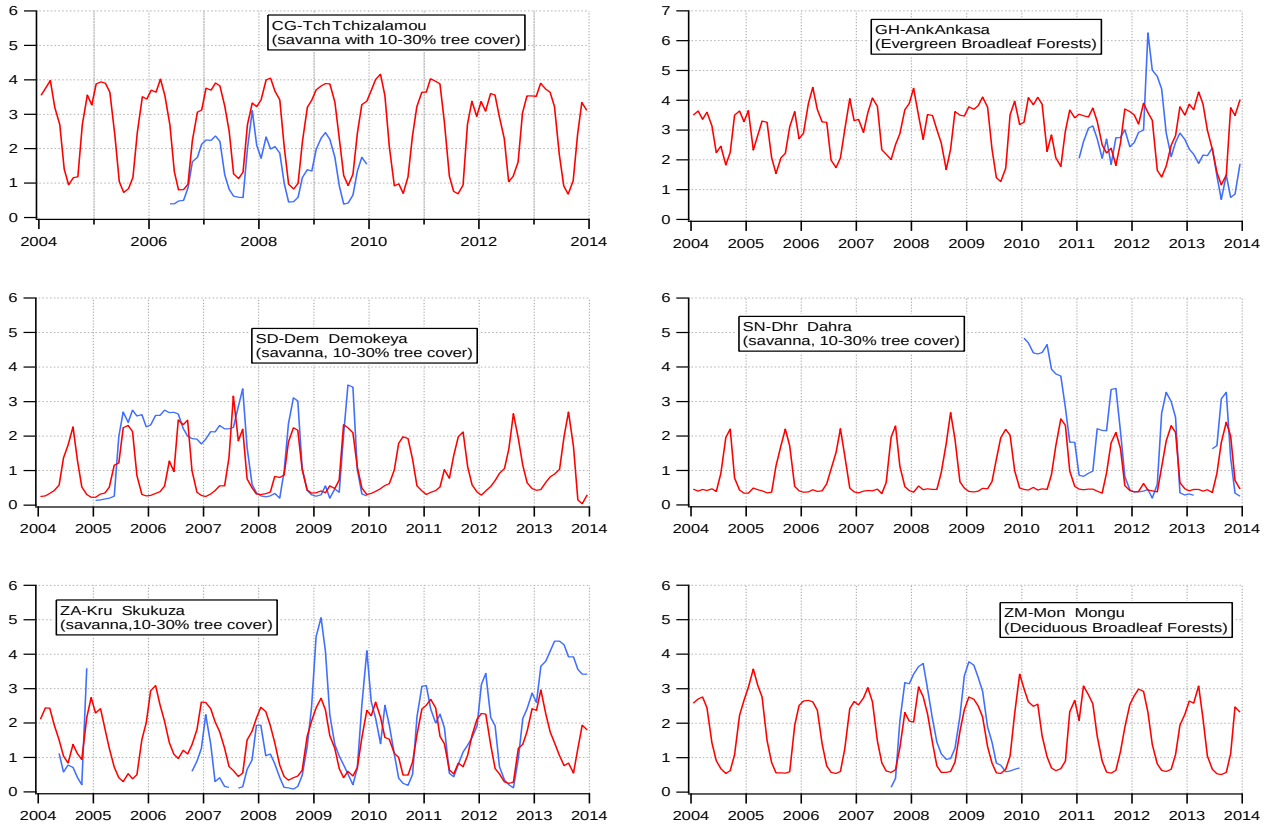

Fig. S5. Continued.

(f) Asia (10 sites)

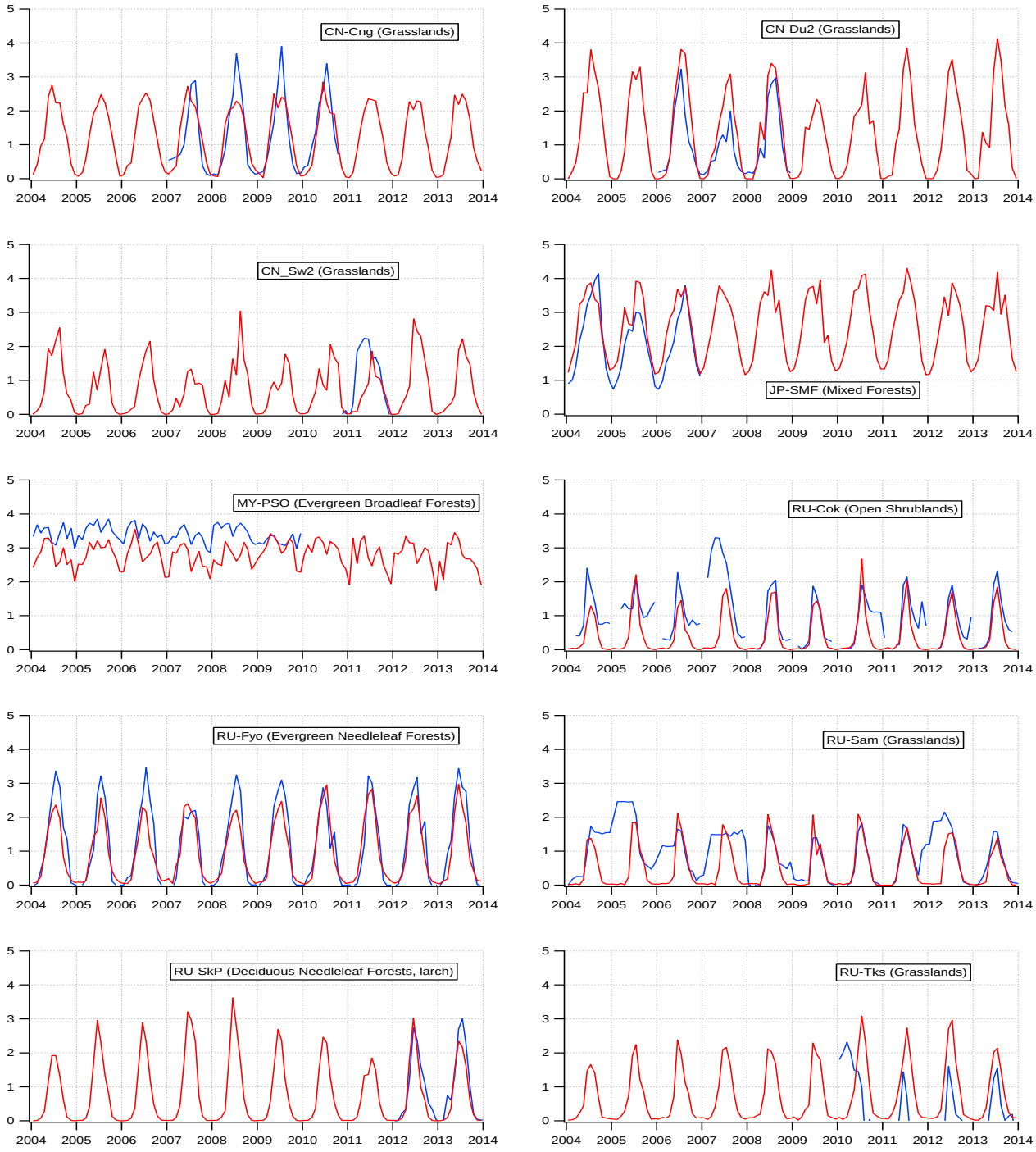

Fig. S5. Continued.

(g) Australia (9 sites)

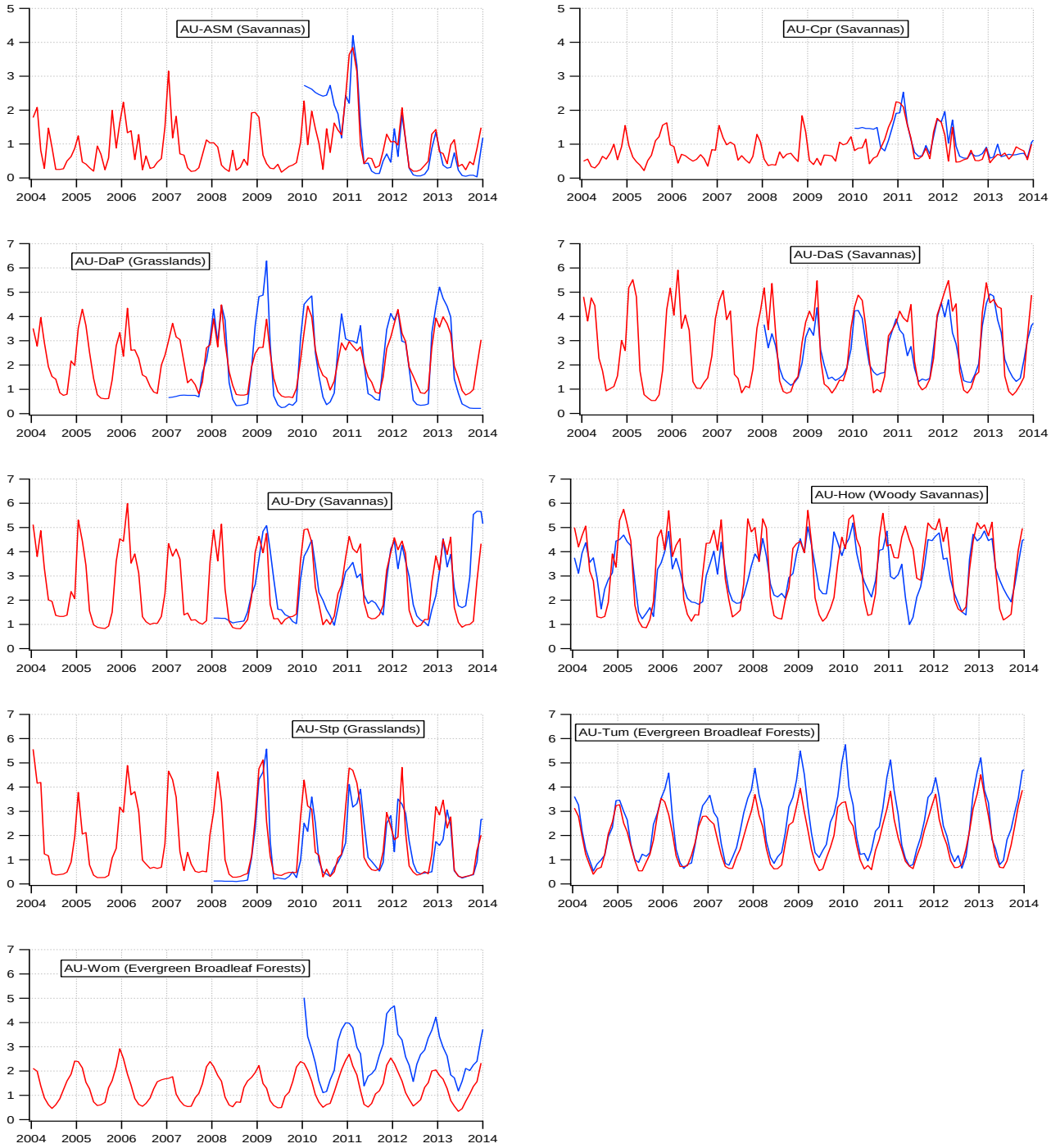

Fig. S5. Continued.

4.2. Comparison of river discharge with gage observations

Fig. S6a displays the 19 major river gauging stations from the Global Runoff Data Center (GRDC, https://www.bafg.de/GRDC/EN/Home/homepage_node.html) in red, which overlap with our model period. Unfortunately, many GRDC records ceased in the late 1990s. We supplemented the GRDC dataset with four gauges from the US Geological Survey (https://waterdata.usgs.gov/nwis/sw) in the Mississippi drainage (green), 10 gauges in the Amazon drainage (orange) from Agência Nacional de Águas e Saneamento Básico (ANA, https://www.ana.gov.br/portal-ingles/monitoring), and one from a published historic reconstruction (black), resulting in 34 gauge records. Figs. S6b-g present monthly comparisons at these sites, organized by continent. Unlike flux tower sites with an average 2km footprint, stream gauge observations reflect integrated hydrologic responses over river basins. The vertical axis plots monthly stream discharge (m^3/s), and the horizontal axis represents years in monthly increments. Observations are shown in blue, and model results in red.

Our model does not account for anthropogenic streamflow alterations, such as reservoir regulation, river diversion for irrigation, or large lakes in river flow routing. Where such processes dominate river flow regimes, our model significantly deviates from observations. The Murray River in southeastern Australia is a notable example, as it is a vital irrigation source for the semi-arid lower Murray-Darling River basin. During the 2004-2010 drought years, when irrigation intensified, streamflow significantly differed from the natural flow our model emulates. Another notable example is the Paraná River in South America, which drains heavily populated areas in Brazil, such as the State of São Paulo, and is thus highly diverted. We present number of upstream reservoirs for the river basins in South America, focus on this study, in Table S3.

In high latitudes, our model does not represent seasonal freezing and thawing of rivers, resulting in a weak seasonal cycle (e.g., larger rivers draining into the Arctic in Russia). Considering no model parameters are calibrated to match observations and our model's primary focus is on exploring hydrologic stress on plants from a variable water table, obtaining accurate evapotranspiration (ET) and its seasonal cycles is more crucial. Thus, we deem the model sufficient for its intended purpose.

(a) The 34 river gages

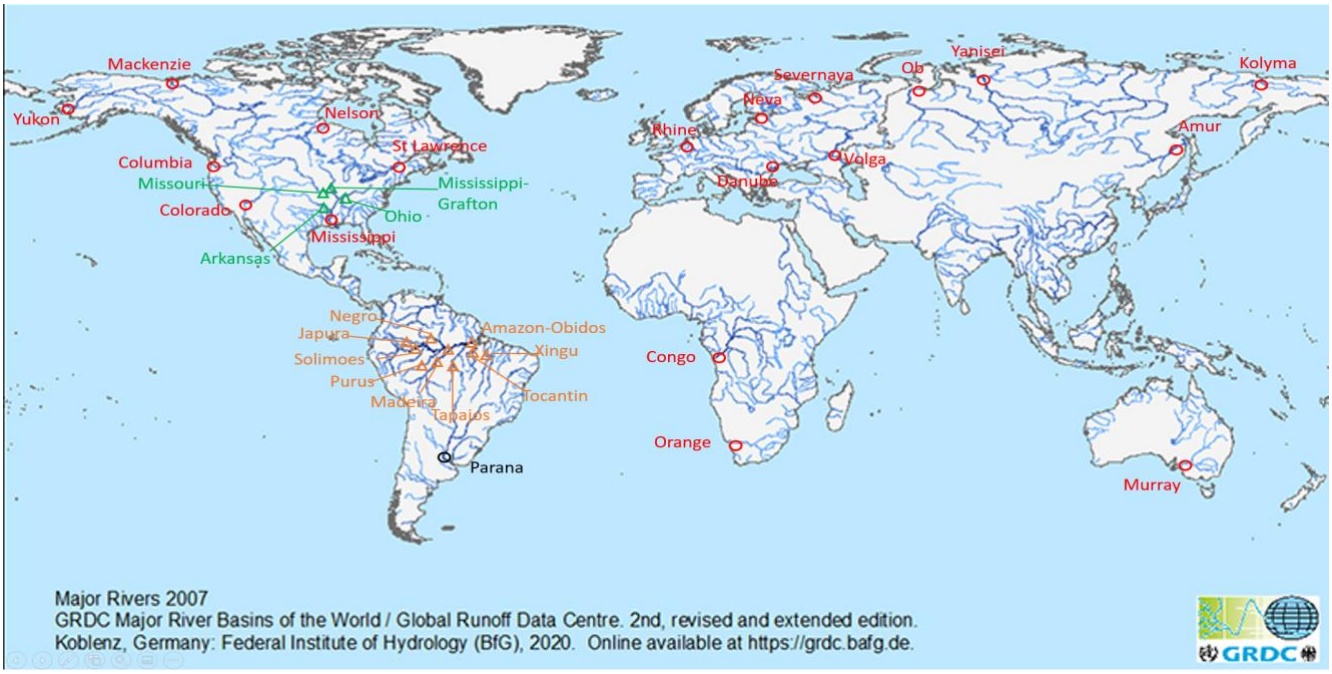

(b) North America (11 river basins)

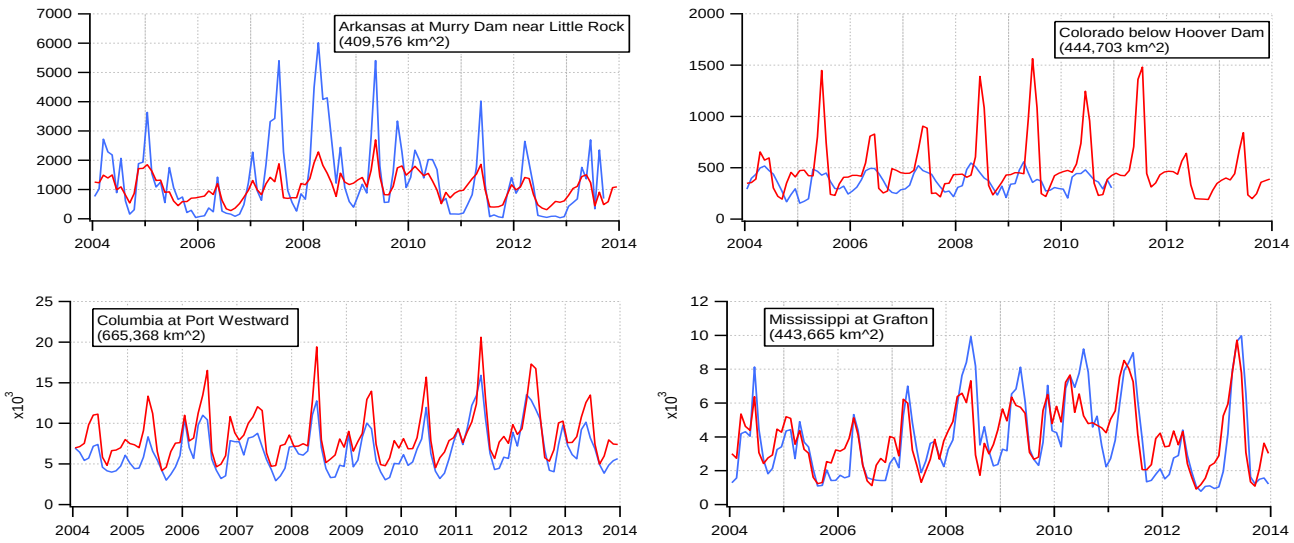

Fig. S6. (a) Location of the 34 river gages used in our global comparison; (b) Comparison between observed (blue) and modeled (red) monthly river discharge (km^3/s).

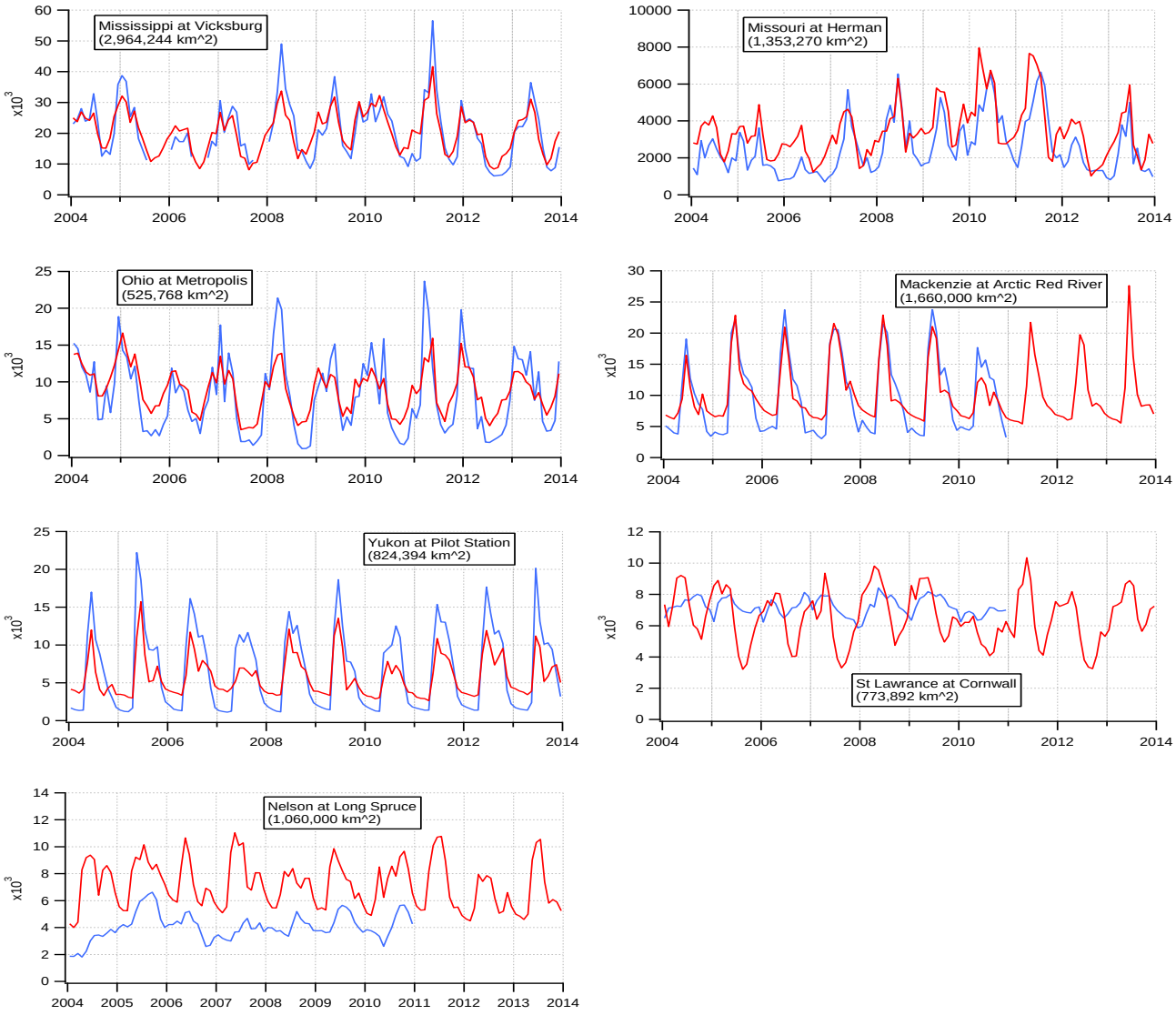

Fig. S6. Continued.

(b) South America (11 river basins)

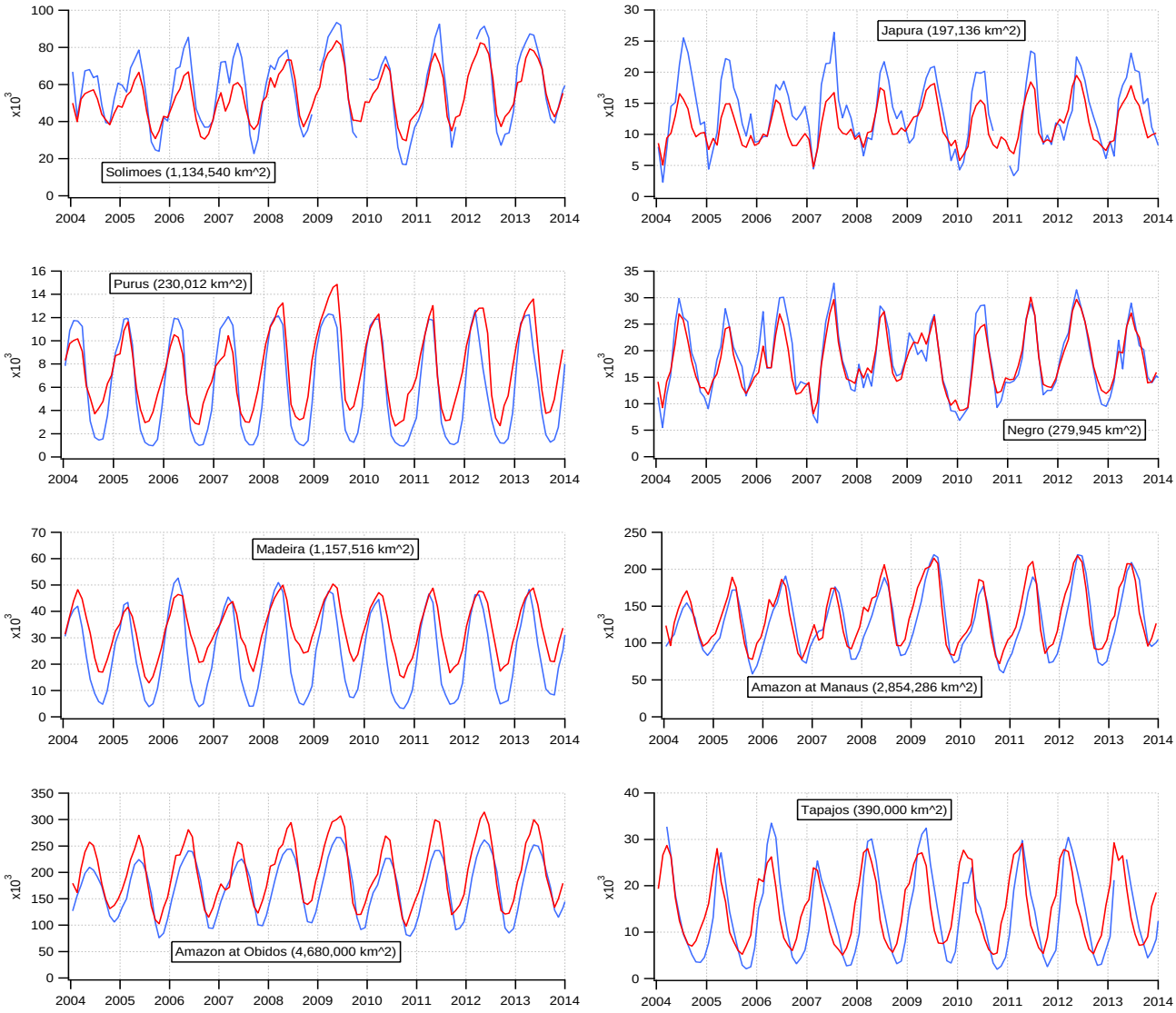

Fig. S6. Continued.

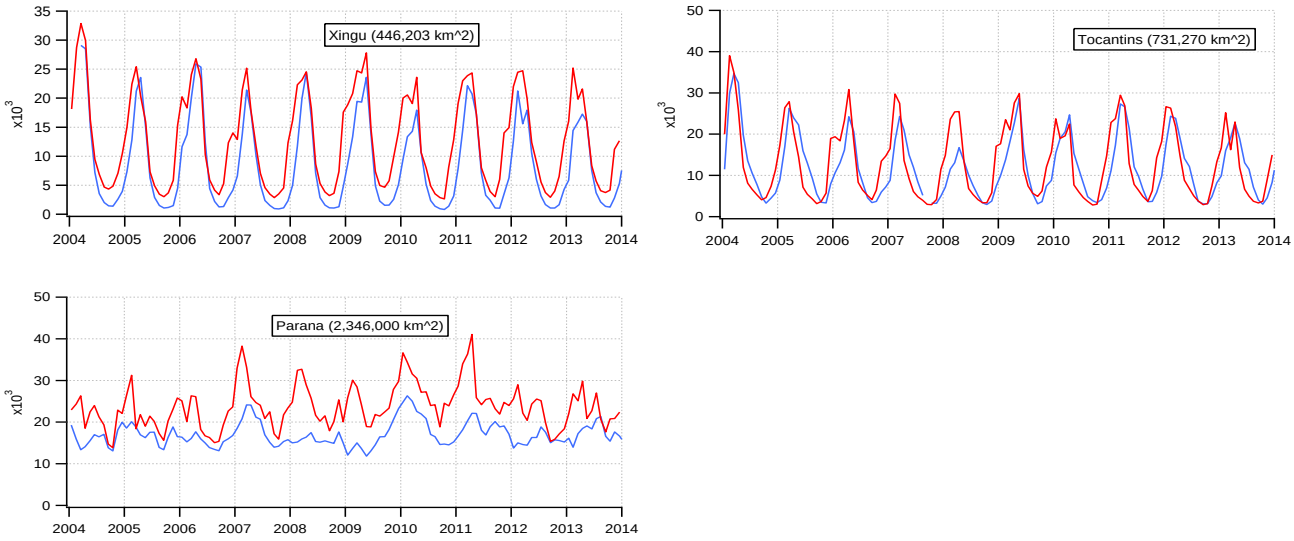

(c) Europe (5 river basins)

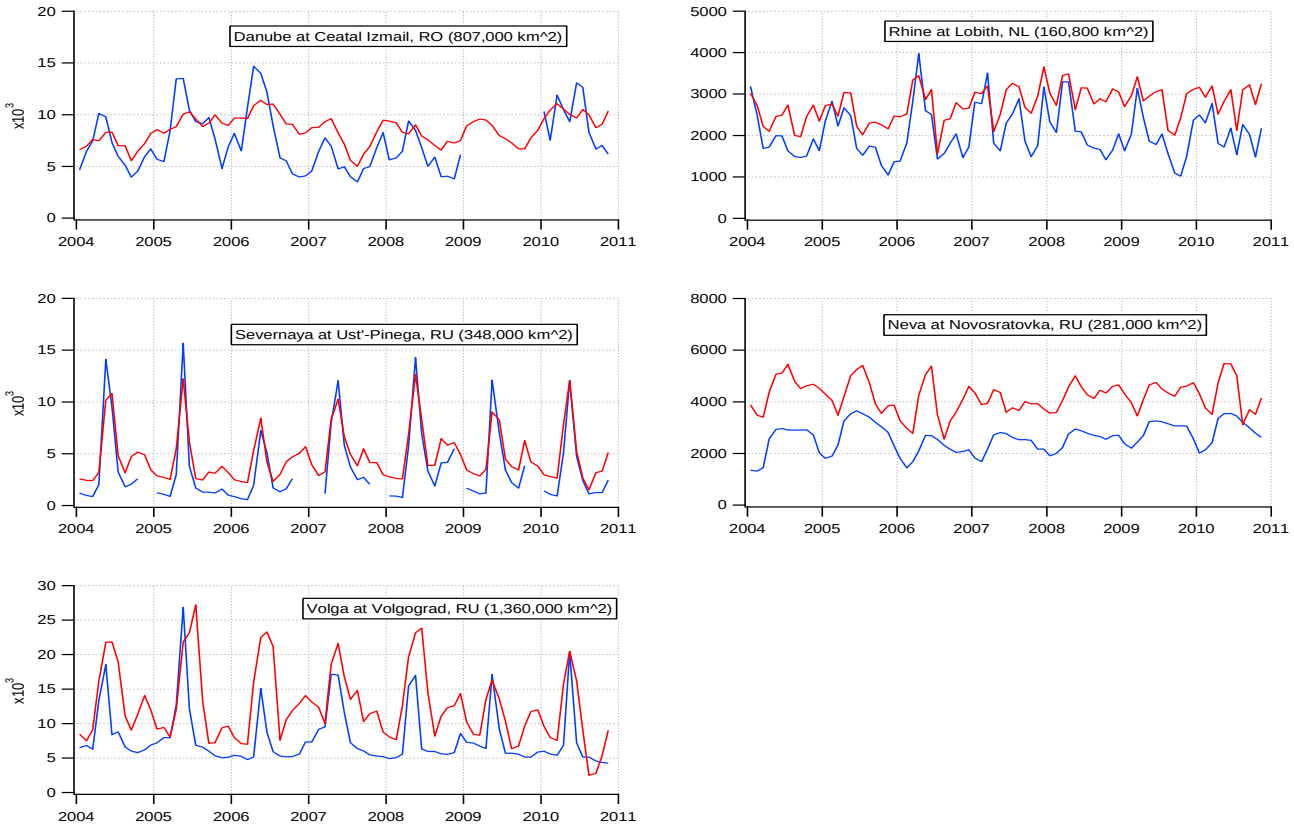

Fig. S6. Continued.

(d) Africa (2 river basins)

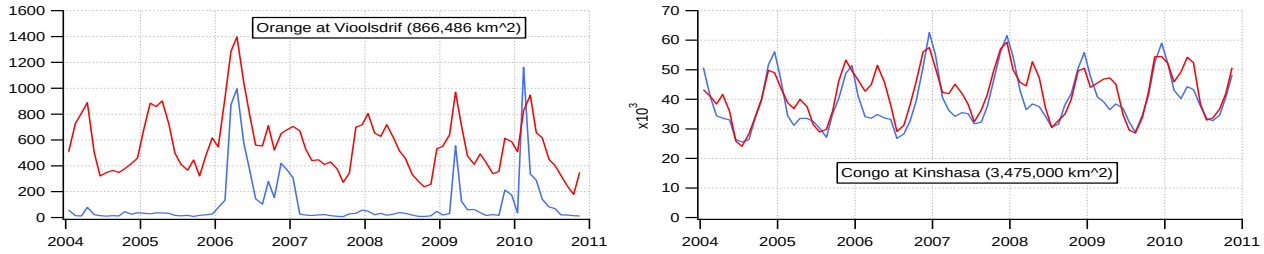

(e) Asia (4 river basins)

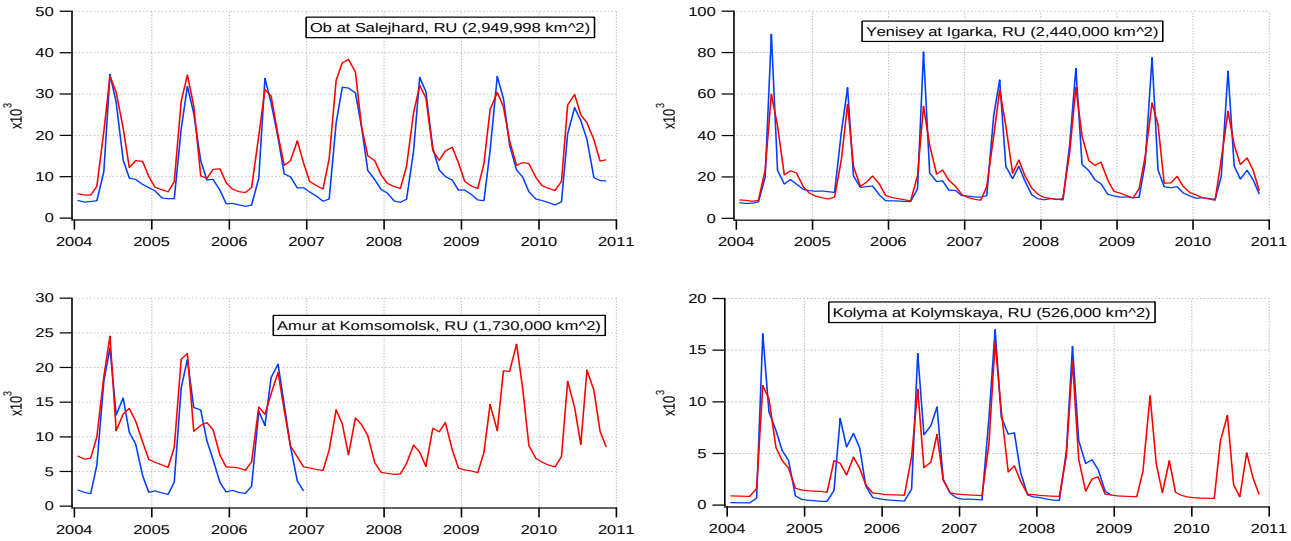

(f) Australia (1 river basin)

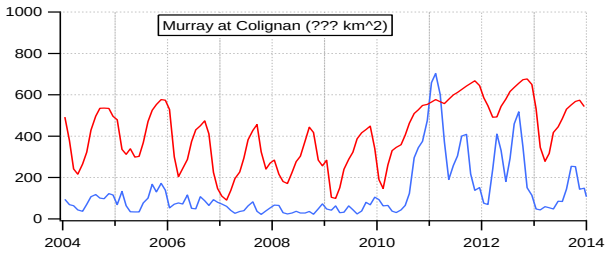

Fig. S6. Continued.

Table S3 – Number of upstream reservoirs of the discharge gages used in the model evaluation (Fig. S6). We combined the stations Solimões, Japurá and Purus because individual data was not available. All data comes from Agência Nacional das Águas (ANA).

Observation stations	Number of upstream reservoirs
Solimões, Japurá, Purus	72
Negro	39
Amazon at Manaus	111
Madeira	685
Amazon at Óbidos	815
Tapajós	2,313
Xingu	2,931
Tocantins	18,061
Paraná	51,470

4.3. Comparison of long-term mean water table depth with groundwater well observations

Here we report a new effort to validate the long-term mean water table depth (WTD) from the simulation used in this study. We compiled well observations for the entire continent of South America (23) from government agencies and the literature. These wells are drilled and sampled in different times and are best used to check our modeled 15 year mean WTD. There is a total of 34,508 point-observations, but they tend to be concentrated around urban centers and agricultural regions where pumping affects the water level. Comparing model output to groundwater well observations is difficult because of the mismatch between scales: a 1x1 km model cell vs a point observation. We filter out observations where the difference between the model grid and recorded land elevations of the well are greater than the range of elevation within a model grid based by high resolution (30 m) DEM. This ensures that the observation and the model are at a comparable topographic position. After applying this filter, we used the remaining 4,885 data points to examine the residuals between observation (h_{obs}) and model mean head (h_{model}). Ideally, the residuals would (a) be normally distributed, (b) have small standard deviation, and (c) have no relationship with topography or climate (systematic bias). Our results (Fig. S7) show that the model

has a higher or shallower water table than observations, which is expected given that most of the groundwater wells are drilled in places of groundwater exploitation and subject to pumping, which lowers the natural water table level (23). We also find low correlations between the residuals and the elevation and MAP, indicating no significant systematic bias along elevation or rainfall gradients. We note that no calibration was performed to improve model-observation fit.

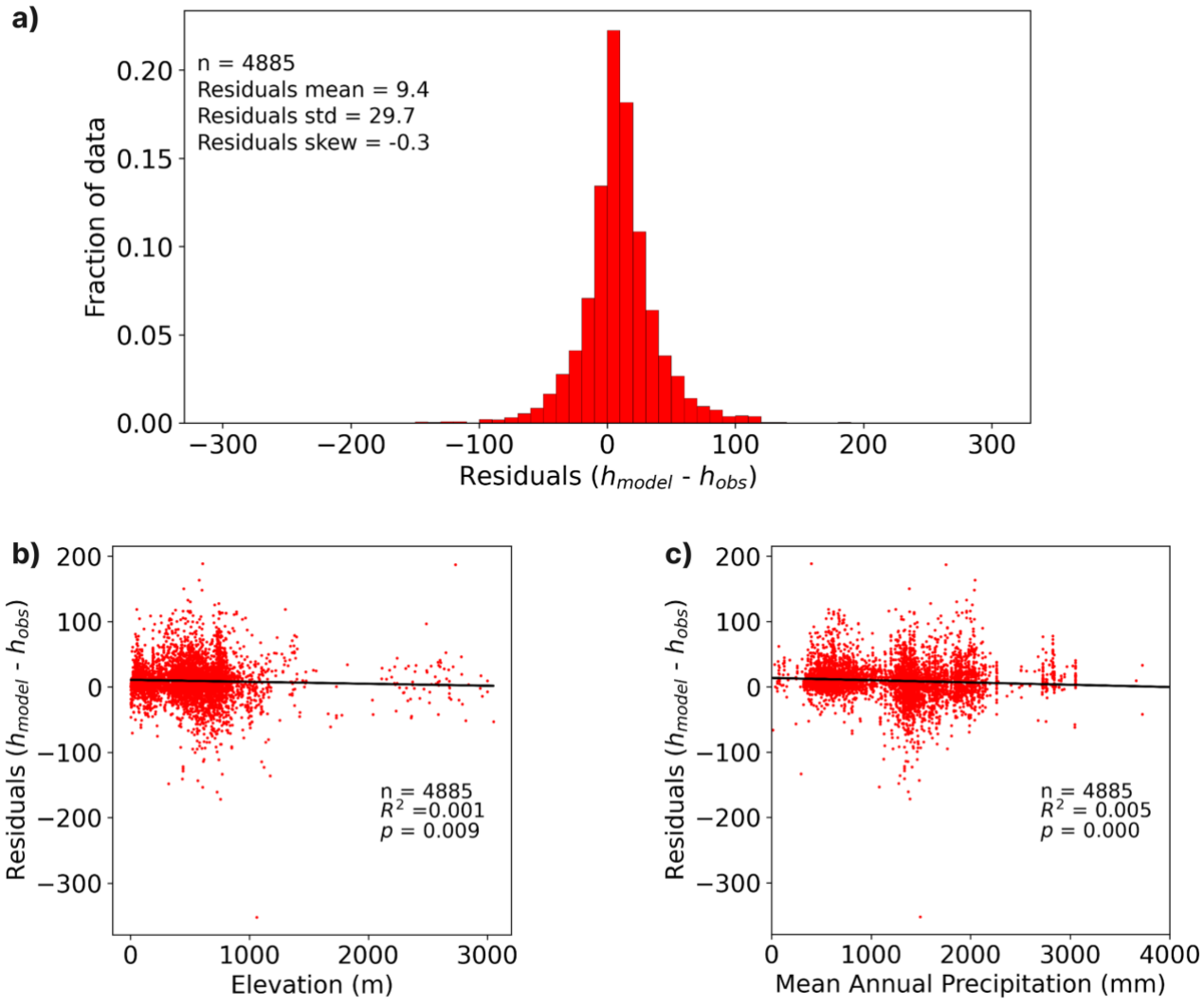

Fig. S7. Validation of mean WTD vs. well observations: (a) histogram of residuals with mean, standard deviation, and skewness; (b) residuals vs elevation; and (c) residuals vs MAP.

4.4. Comparison of monthly water table depth with time series of well observations

We now compare the seasonal cycle of water table to observations. Temporal records of water table depth are even scarcer, and we rely on (i) observations from the Brazilian Geological Survey Integrated Groundwater Monitoring Network (CPRM-RIMAS) in the Amazônia region available at http://rimasweb.cprm.gov.br/ and (ii) a compilation of observations from published literature. Since most of the CPRM-RIMAS wells are deep and tap into rock aquifers, we choose only those measuring free aquifers (no confining layers), with the entire filter section open to sediment (as opposed to rock) and which were not subject to pumping or human water use. This yields a small number of wells, most of which have no temporal overlap with the model simulation period. The same can be said of the observations compiled from the literature, which pose another set of challenges since usually only the general location of the study area is given, instead of the precise coordinates of each well (as in the CPRM-RIMAS wells). To overcome these issues, we (i) average the model and observation timeseries to obtain the seasonal cycle and compare whether the model captures the correct depth and temporal dynamics of the water table; (ii) where precise locations were not available, we choose the closest pixel to each site with similar topographic position as noted in the original source (e.g., elevation or plateau vs slope vs valley) to extract the corresponding model water table. Information and location of observation wells can be found in Table S4 and Fig. S8, and validation plots in Fig. S9.

Table S4. Observations used in water table seasonal cycle comparison

ID	Name	Latitude	Longitude	Start Date	End Date	Source
1	Cruzeiro do Sul	-7.495556	-72.77528	06/2015	11/2020	CPRM-RIMAS
2	Fazenda Catauba	-10.073333	-67.62694	02/1999	12/2004	Selhorst and Brown (2012) (29)
3	Jaú National Park	-1.9125	-61.6375	03/2000	10/2010	Do Nascimento et al. (2008) (30)

4	Reserva Cuieiras	-2.61	-60.2	01/2003	09/2016	Bastos (2019) (31)
5	Óbidos	-1.903333	-55.50861	04/2012	12/2020	CPRM-RIMAS
6	Redenção	-7.83333	-50.26666	12/1996	11/2001	Grogan and Galvão (2006) (32)
7	Bananal Island	-9.821139	-50.148694	11/2003	12/2006	Borma et al. (2009) (33)
8	Belém do Pará	-1.434444	-48.44917	02/2012	05/2021	CPRM-RIMAS

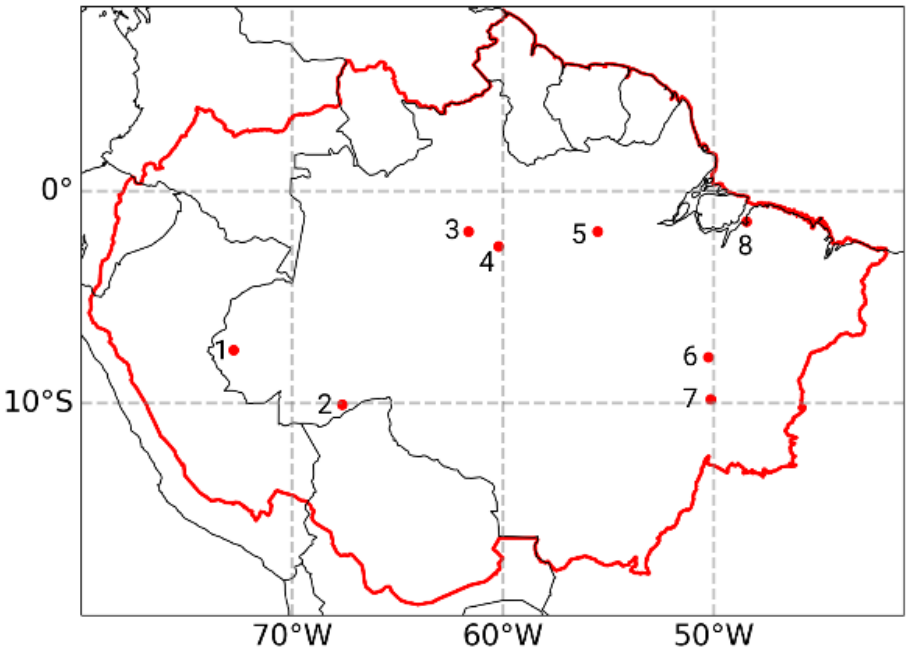

Fig. S8. Location of observations used for water table seasonal cycle comparison. Red lines outline the limits of the Amazônia region.

Cruzeiro do Sul

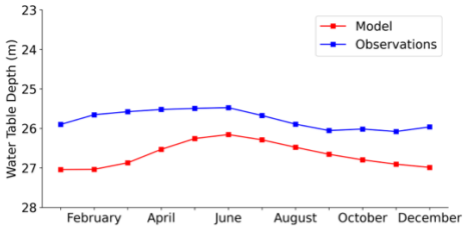

Fazenda Catauba

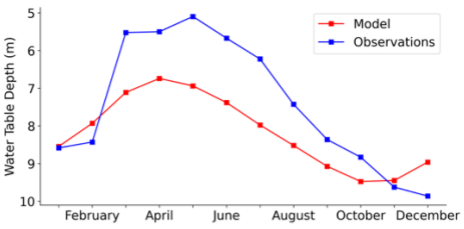

Jaú National Park (Hill)

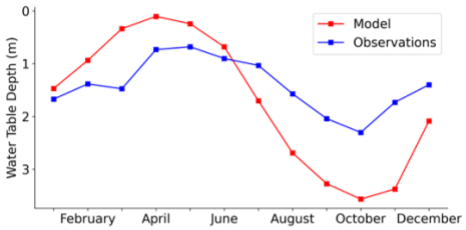

Jaú National Park (Valley)

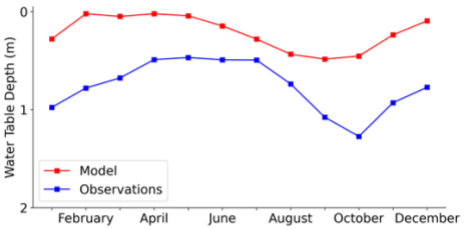

Reserva Cuieiras (Hill)

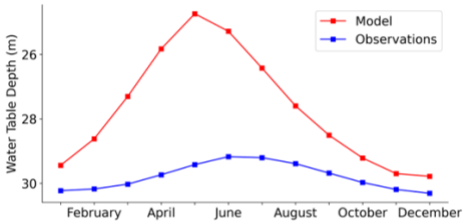

Reserva Cuieiras (Valley)

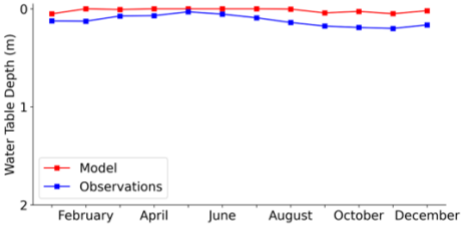

Óbidos

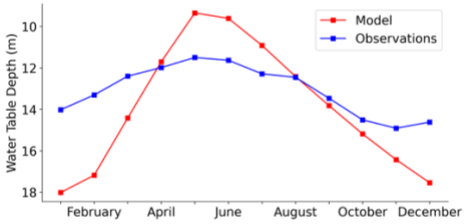

Redenção (Hill)

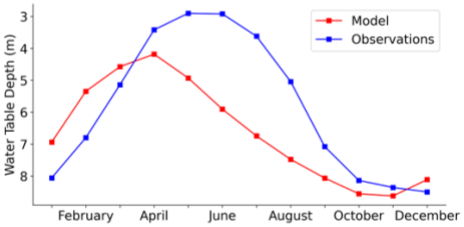

Redenção (Valley)

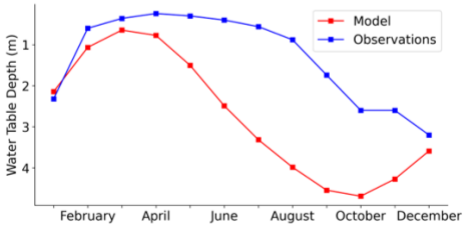

Bananal Island (Hill)

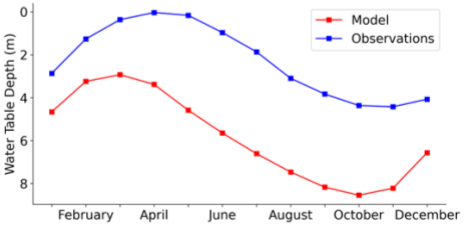

Bananal Island (Valley)

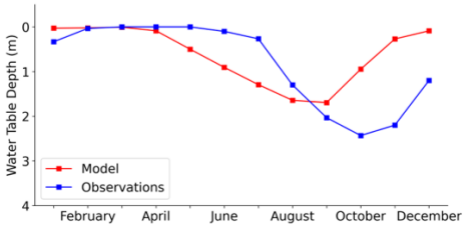

Belém do Pará

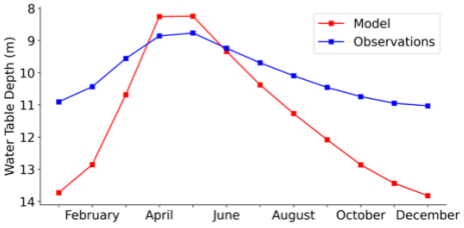

Fig. S9. Comparison between modeled water table depth (in m, red) with observations (blue).

Despite the many uncertainties in the model input data – e.g., soil properties and structure of the subsurface (e.g., permeability), forcing bias and the scale mis-match – the model captures well both the magnitude and the seasonal timing of the rise and fall of the water table across most of the observation sites. The high uncertainties in soil properties can partially explain the differences in variability range between model and observations in some places (e.g., more dampened in Jaú National Park, more variable in Belém do Pará). Vertical and lateral permeability are derived from soil texture(19, 20), and can lead to over or underestimation of the velocity with which water moves through the soil. Furthermore, the low spatial resolution (1km vs a point at a well) also contributes to the dampening of the seasonal cycle, erasing topographic positions such as lower slopes, where the variability of water table is high. Despite these issues, the model consistently represents the spatial and temporal characteristics of hydrology across different geological domains and rainfall regimes, thus reinforcing its usefulness in representing hydrologic states in Amazônia.

4.5. Comparison of terrestrial water storage with GRACE

Because groundwater observations, especially in time, are sparce across Amazônia, we turn to the GRACE satellite products to assess the ability of our model to represent seasonal water storage change across Amazônia. The GRACE mission's monthly mass field products allow for the calculation of temporal changes in terrestrial water storage (TWS), an integrated measure of water stored in different components of the Earth system (34, 35). The product is offered monthly at a 1°x1° spatial resolution from mid-2002 to mid-2017. Our model estimates of TWS anomalies have been shown to agree well with those of GRACE (28) before. Subsurface storage (water in vadose zone + groundwater) has been shown to dominate the TWS signal across most of Amazônia(28), except for areas such as the Rio Negro, characterized by extensive lowlands with a shallow and stable water table, where superficial storages (rivers and floodplains) dominate. Thus, the GRACE product offers us the possibility of evaluating the model's ability to correctly track subsurface water with a spatiotemporal coverage that observations alone cannot provide. Here we adopt a similar comparison procedure focusing on 6 ecoregions of Amazônia. We use model simulations at the 2-km grid scale and compare model estimates of TWS anomalies relative to the 2004-2010 baseline to those of GRACE (36) in the same time period (Fig. S10).

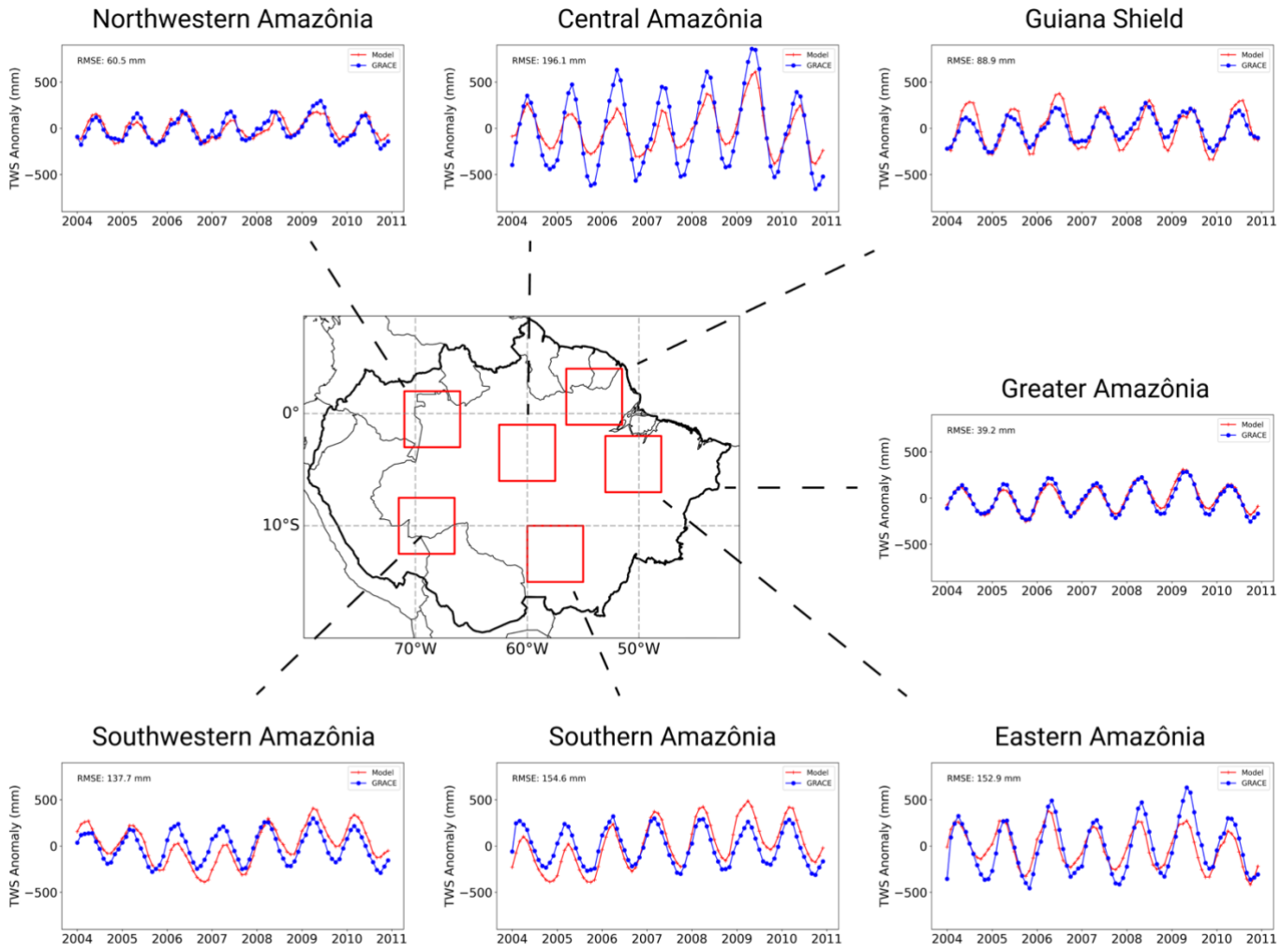

Fig. S10. Comparison of simulated terrestrial water storage with GRACE satellite data for the entire Amazônia and 6 ecoregions in the basin.

Our results show that the model correctly reproduces both the magnitude and seasonality of TWS change for the entire Amazônia region and each ecoregion of interest. We note that the dampened seasonal cycle in regions like Central Amazônia can be attributed to the well documented bias in the precipitation forcing in earlier versions of the ERA-Interim project, with too much rain in the dry season and too little in the wet season (19, 20, 28). This bias has since been corrected and incorporated into the ERA5 version of the reanalysis used to force the model in our current study. Nonetheless, we show that the model can correctly track the magnitude and timing of the movement and storage of water across many reservoirs on land without any calibration and is thus suitable for the purposes of our study.

5. Measuring hydrologic stress

We define three drainage classes (see Fig. 1b) to represent distinct hydrologic environments or niches using a 2m threshold as a rough guidance on rooting depth and 0.25 m as a threshold for waterlogging stress. Rooting depth remains a vastly under sampled plant trait, and observations and model results show that it can vary greatly following topography, climate and species(21). Therefore, defining a unique threshold as accessible versus inaccessible water table is difficult. We argue that the 2 m threshold is sufficient to capture the difference between the shallow rooting herbaceous plants which make up the majority of savannas biomass, and deep rooting forest species on well-drained hillslopes and plateaus. Moreover, a compilation of over 2,000 observations of rooting depth shows that ~70% of all observations are shallower than 2 m (21), which gives us confidence that this is a meaningful biological threshold to define groundwater access. Previous work shows that the 0.25 m threshold gives the best representation of mapped wetlands in North America (26). In a Brazilian hyperseasonal savanna, shallow water tables were shown to decrease woody species abundance (37–39), and no woody species were reported to survive to adulthood where the water table was within the top 20 cm of soil (37). Comparison with simulations of flooding frequency show that the 0.25 m threshold mirrors flooding frequency, and for 87% of pixels, yields higher waterlogging stress frequency than flooding alone (Fig. S11), making it a more powerful indicator than flooding alone. Therefore, we consider that a water table in the top 0.25 m of soil is enough to cause oxygen stress to the bulk of plant roots.

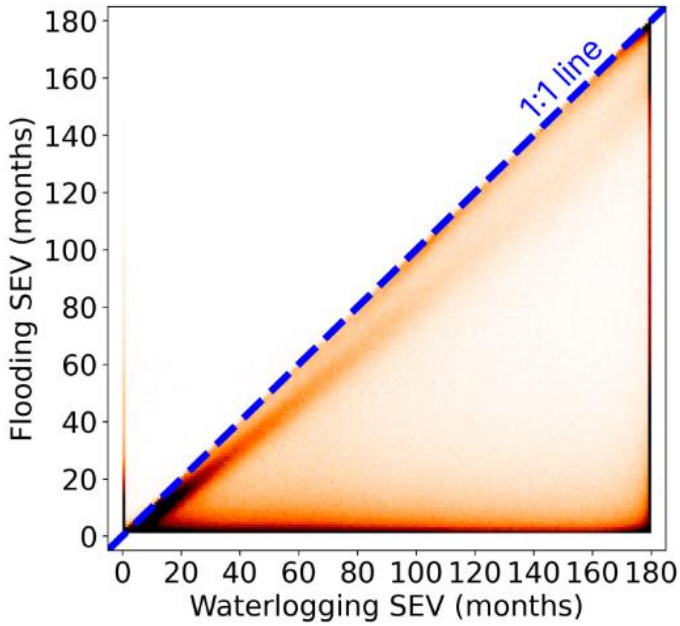

Fig. S11 – 2-D histogram showing the distribution of pixels in the study area regarding their waterlogging and flooding stresses. The horizontal axis shows waterlogging sum exceedance value (SEV), calculated as the number of months with water table above 0.25 m, while the vertical axis shows flooding SEV, calculated as the number of months with a water column above the soil surface. Darker colors indicate a higher concentration of pixels in each bin.

Following the hydrologic niche theory of Silvertown et al. (1999) (40), we compute the sum exceedance values (SEV) to quantify the frequency of waterlogging and drought stress experienced at each landscape position. We define the drought stress SEV (Fig. S12) as the average number of months per year (over 15 years) in which the water table is below the 2 m threshold defined above. The waterlogging SEV (Fig. S13) is defined as the number of months with water table above 0.25 m. The "deep water table (drought stress)" class has pixels in which the water table is always below the 2 m threshold, and therefore a drought SEV value of 12 months. The "alternating shallow and deep water table (double stress)" class has pixels in which the water table rises above 0.25m in the wet season but falls below in the dry season, characterizing highly dynamic locations, and have drought and waterlogging SEVs greater than 1 month; the "shallow water table (waterlogging stress)" class has pixels in which the water table is always above 0.25 m and imposes permanent waterlogging stress, with a waterlogging SEV value of 12 months. For each combination of the three water table and three precipitation (from potential

analysis above) classes, we compute the tree cover distribution and the relative abundance of forest versus savannas on an area basis (Fig. 1b).

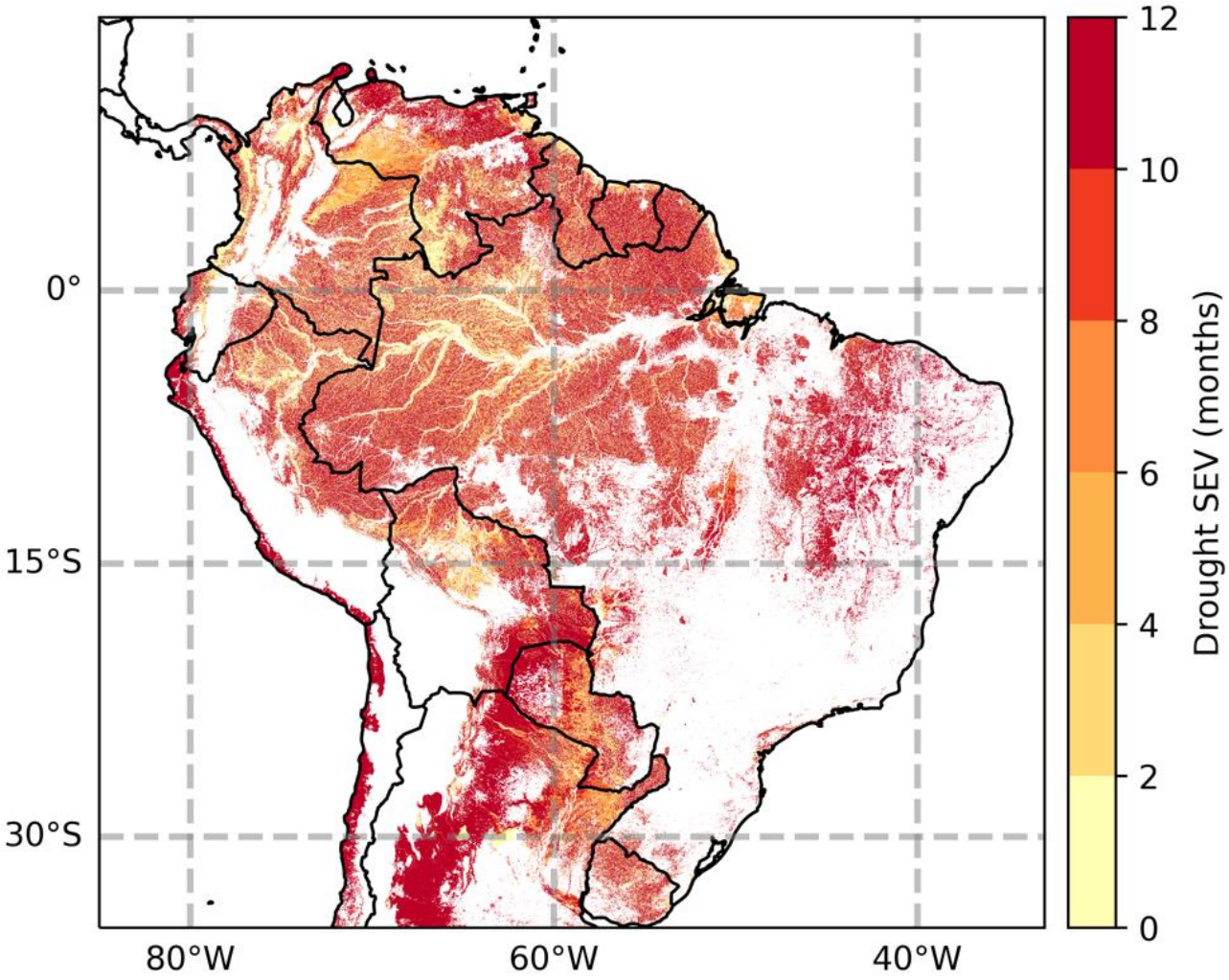

Fig. S12 – Drought sum exceedance value (SEV), calculated as the average number of months with WT deeper than 2m. White pixels correspond to areas excluded from analyses (e.g., open water, agriculture, high elevations).

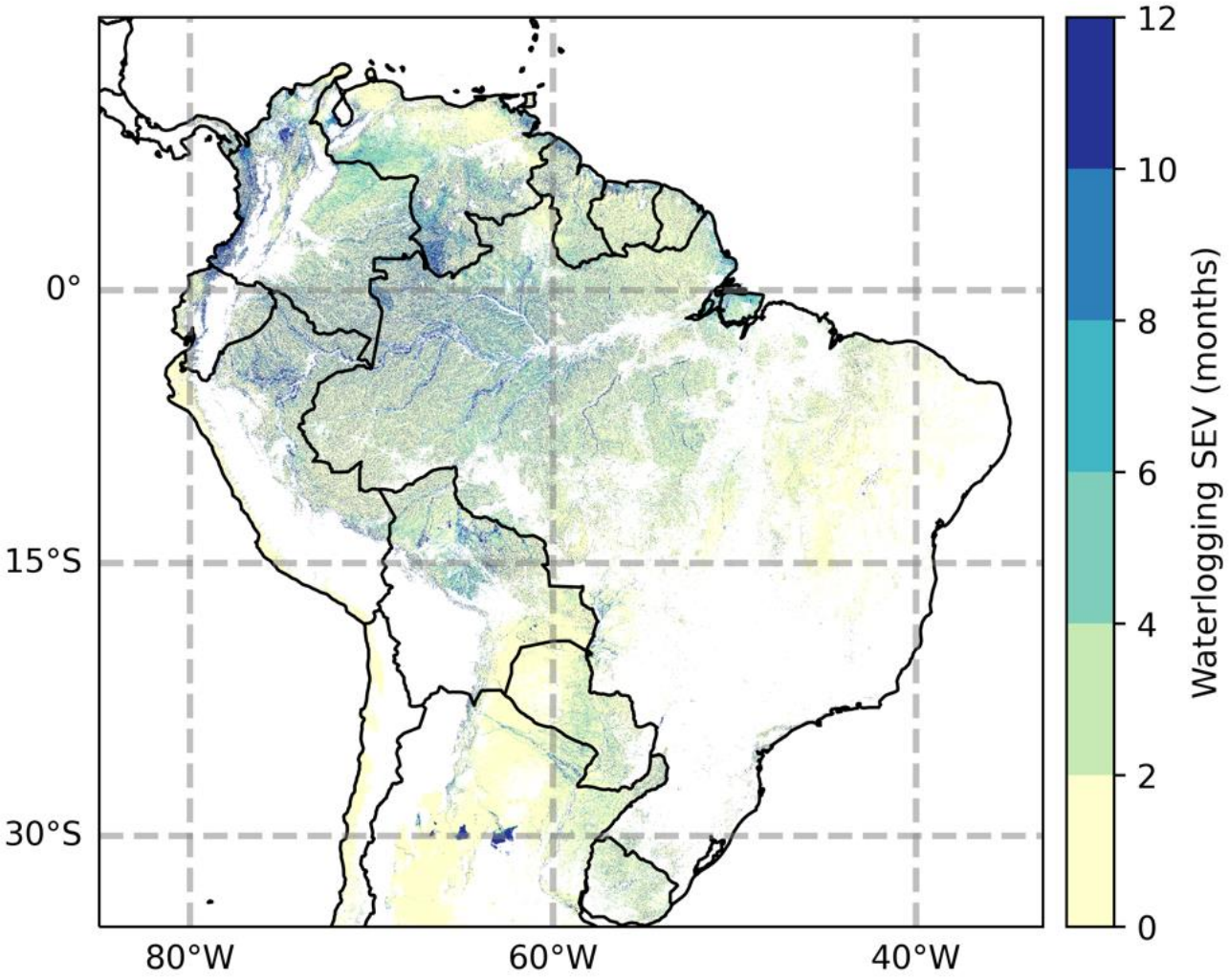

Fig. S13 – Waterlogging sum exceedance value (SEV), calculated as the average number of months with WT shallower than 0.25 m. White pixels correspond to areas excluded from analyses (e.g., open water, agriculture, high elevations).

To construct Fig. 2b, for each possible waterlogging/drought SEV combination, we select all valid model pixels which have that specific combination and calculate forest proportion as the ratio of forest pixels' area to the area of all pixels (forests and savannas) inside that bin (Fig. 2b). If all pixels in a specific SEV combination are covered by forest vegetation, forest proportion is 100%. If all pixels are savannas, then forest dominance is 0%.

We also determine the double stress index (DSI) as the harmonic mean of waterlogging stress SEV and drought stress SEV (Fig. S14). DSI ranges from 0, where there is no double stress, to 6, representing the

maximum double stress intensity of 6 months of drought followed by six months of waterlogging. We use the DSI to create three classes of double stress: no double stress (DSI = 0), weak double stress (0 < DSI < 4) and strong double stress (DSI > 4). We use these classes to categorize each land pixel into one of three classes and plot them in Fig. 2c.

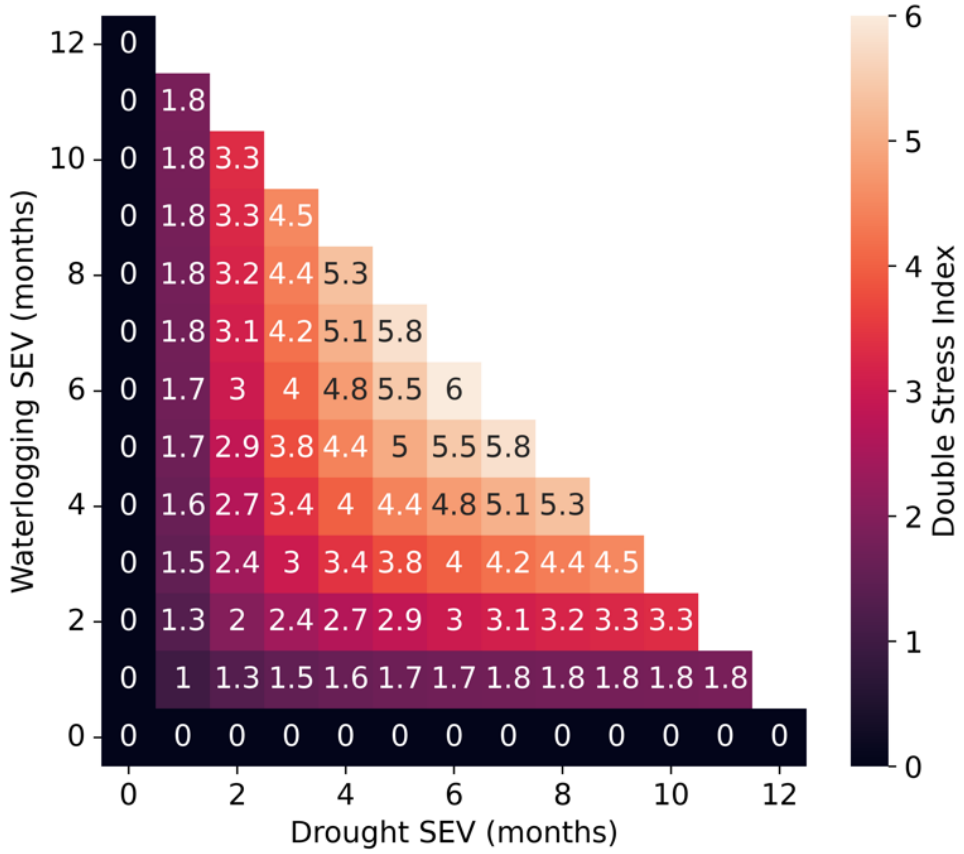

Fig. S14 – Values of the Double Stress Index (DSI) for each waterlogging and drought sum exceedance value (SEV) bin. Values range from 0, where there's no stress or only waterlogging/drought stress, to 6, where both waterlogging and drought SEVs equal 6 months.

In Fig. 3, for each of the six insets, we calculate the distribution of tree cover using seaborn's *KDEplot* function for two drainage classes: non-double stressed and double stressed, defined using the DSI index described above. To obtain the seasonal cycle of precipitation and WTD, we use ERA5-Land precipitation averaged for all pixels in each region, and model WTD data average for all waterlogged pixels (at least one month of WTD shallower than 0.25 m) in each region. We show in Table S5 below

the proportion of forest and savanna in each drainage condition (non-double stressed or double stressed) for all six floodplains.

Table S5 – Proportion of forest and savanna in each drainage condition (non-double stressed or double stressed) for the six floodplains shown in the Fig. 3 of the main text.

Location	Condition	Forest (%)	Savanna (%)
Pastaza-Marañón Foreland Basin	Non-double stressed	96	4
	Double stressed	96	4
Marajó Island	Non-double stressed	87	13
	Double stressed	55	45
Llanos de Orinoco	Non-double stressed	3	97
	Double stressed	1	99
Llanos de Moxos	Non-double stressed	16	84
	Double stressed	8	92
Bananal Island	Non-double stressed	6	94
	Double stressed	4	96
Pantanal	Non-double stressed	5	95
	Double stressed	3	97

6. Sensitivity and statistical analyses

To test whether our results on savanna-forest distribution in the double-stress space are robust to errors/biases in the modeled water table dynamics, we perform a sensitivity analysis using the water table data. First, to assess the magnitude of the biases, we use the groundwater monitoring wells with available time series to estimate the average monthly error between observation and model in magnitude, and also a possible displacement in time (lag) between model and observations (Fig. S15) below. Our results show that the model has a mean error of – 0.58 m (deeper than observations), and while 11 points had no lag between model and observations, one point (Bananal Island valley) did show a 2-month lag between both.

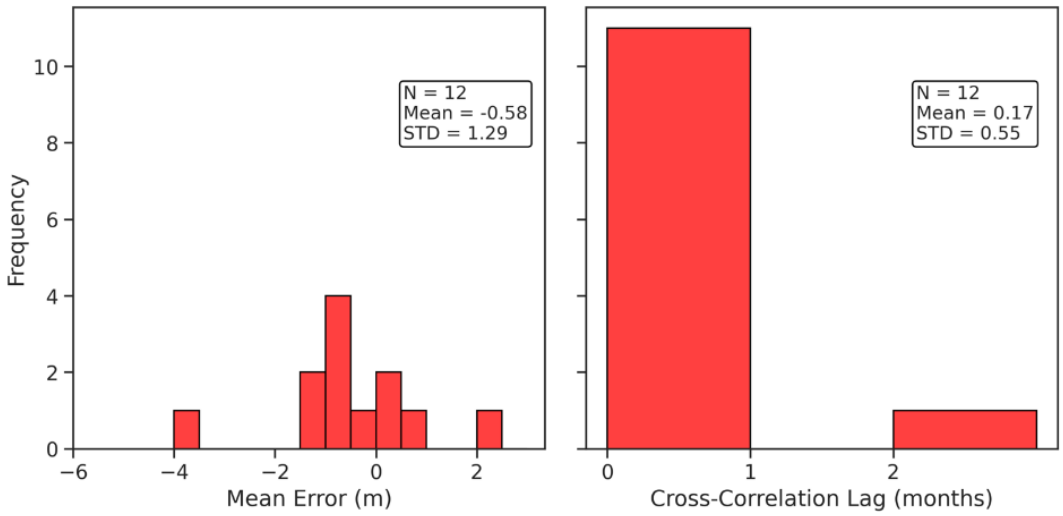

Fig. S15 – Statistics for comparison between modeled and observed water table depth. We show the distribution of mean error (observation – model) for all wells in (a) and also the distribution of temporal lag between observations and model in (b).

With these results, we then design two analyses to test the sensitivity of our results to these biases: (1) a shallower water table analysis, adjusting the model water table by the mean error (0.58 m above) and (2) a lagged water table, moving the temporal series by 2 months (representing the highest observed lag). The results of forest/savanna proportions in drainage and rainfall classes (as shown in Fig. 1 in the paper) show minor changes in the shallower WT analysis, and no change in the lagged WT analysis (Table S6 below).

Table S6 – Sensitivity analysis results of forest and savanna proportions according to rainfall and drainage classes (comparable to Fig. 1 in main text). Green color indicates increase compared to original run; red indicates decrease and yellow indicates no change.

Rainfall	Drainage	Simulation	Forest (%)	Savanna (%)
Low rainfall	Deep water table	Original	5.7	94.3
		Adjusted, shallower WT	5.8	94.2
		Adjusted, lagged WT	5.7	94.3
	Alternating water table	Original	5.2	94.8
		Adjusted, shallower WT	4.5	95.5
		Adjusted, lagged WT	5.2	94.8
	Shallow water table	Original	9.9	90.1
		Adjusted, shallower WT	12.3	87.7
		Adjusted, lagged WT	9.9	90.1
Intermediate rainfall	Deep water table	Original	50.4	49.6
		Adjusted, shallower WT	51.3	48.7
		Adjusted, lagged WT	50.4	49.6
	Alternating water table	Original	23.6	76.4
		Adjusted, shallower WT	22.7	77.3
		Adjusted, lagged WT	23.6	76.4
	Shallow water table	Original	50.1	49.9
		Adjusted, shallower WT	50.6	49.4
		Adjusted, lagged WT	50.1	49.9
High rainfall	Deep water table	Original	87.5	12.5
		Adjusted, shallower WT	87.6	12.4
		Adjusted, lagged WT	87.5	12.5
	Alternating water table	Original	68.5	31.5
		Adjusted, shallower WT	69.7	30.3
		Adjusted, lagged WT	68.5	31.5

	Shallow water table	Original	84.9	15.1
		Adjusted, shallower WT	86.6	13.4
		Adjusted, lagged WT	84.9	15.1

We then test whether the patterns of forest/savanna dominance in the SEV space (Fig. 2 in the manuscript) were sensitive to the two changes in WT (Fig. S16 below). Our results show that while some pixels changed in the shallower WT run, the pattern of increased savanna dominance as double stress increases (diagonally from the origin) remains the same. There were no changes for the lagged WT analysis.

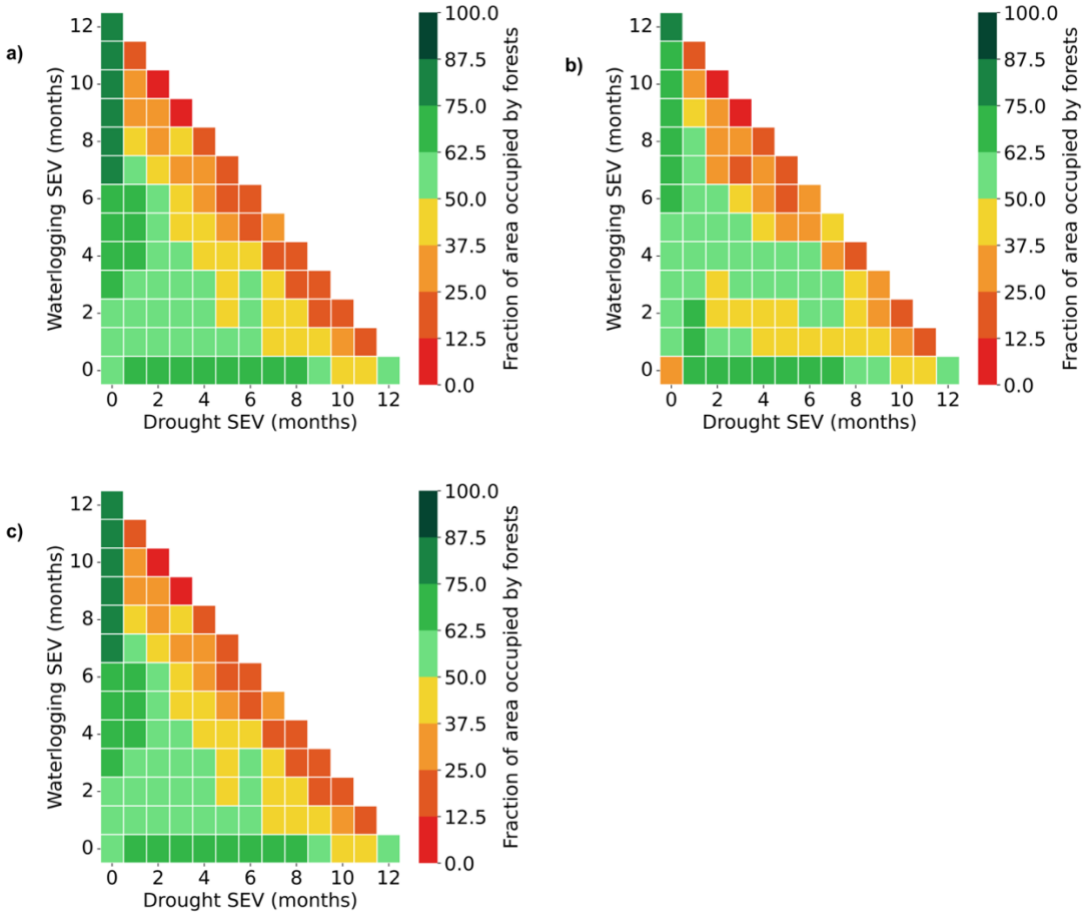

Fig S16 – Comparison of forest-savanna proportion in the 2-D sum exceedance value (SEV) space. The horizontal axis represents the frequency of drought (water table deeper than 2 m, in months), while the vertical axis represents the frequency of waterlogging (water table shallower than 0.25 m, in months).

We show the results for the (a) original water table, (b) adjusted, shallower water table and (c) adjusted, lagged water table.

To statistically test the combined effects of mean annual precipitation, seasonality, and double stress on the existence of forest and savanna, we first model log-transformed tree cover using a Generalized Least Squares (GLS) linear model, assuming normally distributed errors, with increasing complexity of predictors. We start with mean annual precipitation (MAP) as the only predictor. We then add the seasonality of rainfall, measured using the relative entropy index (41, 42). The relative entropy measures how different a pixel's mean monthly precipitation is from the uniform distribution (MAP equally distributed through the year), thus giving us a seasonality measure that does not rely on assumptions regarding the definition of dry season rainfall totals, the start of the dry season or ET rates, such as the MCWD (43). Finally, we add the Double Stress Index (DSI) as a predictor, calculated as described above. All predictors had low Variance Inflation Factor (VIF), between 1 and 1.5 (see Table SX below), suggesting low multicollinearity and therefore suitability to be employed as independent predictors in our model.

Table S7 – Variance Inflation Factor (VIF) for the predictor environmental variables used to predict tree cover.

Environmental variable	**VIF**
Mean Annual Precipitation (MAP) (mm yr^{-1})	1.418
Relative Entropy of Precipitation (RE)	1.411
Double Stress Index (DSI)	1.01

Our results (Table S8) show that the model with 3 predictors (MAP, RE and DSI) has the best performance, measured by the Akaike Information Criterion (AIC), the Bayesian Information Criterion (BIC) and the Adjusted-R^2. Moreover, the coefficients of the best model (Table S9) show that MAP has the first and strongest control on tree cover, followed by seasonality and double stress. Seasonality and double stress have similar coefficients, and both show a negative relation with tree cover (decreasing tree cover with increasing rainfall seasonality and increasing double stress, as stated in our paper). The

other models show that, out of all the predictors, MAP has the best performance compared to seasonality and DSI, which is consistent with the argument that rainfall drives the large-scale changes in tree cover, while seasonality and especially the groundwater-induced double stress control finer-scale features.

Table S8 – Performance metrics for the Generalized Least Squares (GLS) models of tree cover as a function of one or multiple environmental variables. Models are sorted from the best (based on lowest AIC value) to worst.

Formula	AIC	BIC	Adjusted R^2
log(tree cover) ~ MAP + RE + DSI	4.757e6	4.757e6	0.452
log(tree cover) ~ MAP + DSI	4.846e6	4.846e6	0.447
log(tree cover) ~ MAP + RE	4.900e6	4.900e6	0.444
log(tree cover) ~ MAP	4.999e6	4.999e6	0.439
log(tree cover) ~ RE + DSI	8.674e6	8.675e6	0.178
log(tree cover) ~ RE	8.697e6	8.697e6	0.176
log(tree cover) ~ DSI	1.053e7	1.053e7	0.001

Table S9 – Coefficients for the best Generalized Least Squares (GLS) model of tree cover as a function of mean annual precipitation, relative entropy of precipitation and double stress index.

Variable	Coefficient	P value
Intercept	0.987	< .0001
MAP	0.261	< .0001
RE	-0.035	< .0001
DSI	-0.038	< .0001

Second, we define three classes of double stress: no double stress (no stress or single waterlogging/drought stress, DSI = 0), weak double stress (DSI ranging from 0 – 4, or 4 months of waterlogging + 4 of drought) and strong double stress (DSI ranging from 4 – 6, or 6 months of waterlogging + 6 of drought). We then compare the distribution of tree cover in each class (Fig. S17). We test the difference in median values of tree cover between classes using the Mann-Whitney-Wilcoxon

two-sided test. Our results show that median tree cover decreases with increasing double stress, and the median tree cover values in each group are statistically different from one another. However, we do point out that all three classes have large variability in tree cover, stemming from the complexity behind the determinants of tree cover. As the model above shows, low tree cover can be caused by low precipitation, high seasonality, high double stress, or a combination of the three. Moreover, there are other controls on tree-savanna coexistence that we do not account for in this paper, such as fire occurrence and soil nutrient composition (44, 45). Even with these limitations, our results show that double stress is a statistically significant predictor of tree cover, favoring the occurrence of low tree cover where double stress is high.

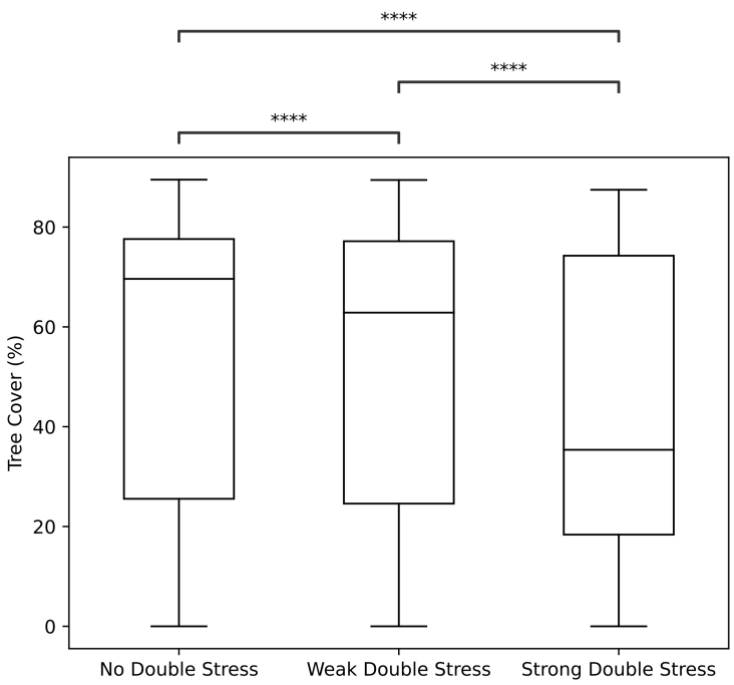

Fig S17 – Tree cover distribution for three double stress classes: no double stress (no stress or only drought or waterlogging stress), weak double stress (double stress index from 0 to 4) and strong double stress (double stress index higher than 4). Whiskers extend to 1.5 times the interquartile range, and horizontal line represents the median value of tree cover in each group. While all three classes have similar ranges of variability, median tree cover is significantly lower especially in the strong double stress class. Asterisks denote statistical significance from a two-sided Mann-Whitney-Wilcoxon test. ****: $p < 0.0001$.

7. Future hydrologic simulation

To explore potential future shifts (Fig. 4), we use two hydrologic simulations at the end of 20th and 21st century (19, 20, 46). These earlier runs are at a coarser resolution (~2km) and did not simulate dynamic rooting depth but solved the full momentum equation in river and floodplain routing, reproducing backwater effects and floodplain inundation important in Amazônia (47). We contrast between a historical simulation for 10 years at the end of the 20th century, and a future simulation for 10 years at the end of the 21st century. Both simulations were forced with output from the Hadley Center Global Environment Model version 2 (HadGEM2-ES). The Hadley Center model is one of the most accurate models in representing precipitation and temperature fields in Amazônia (48), albeit with a wet bias in the southwest and a dry bias in the northeastern wet season (46). The future simulation uses the Representative Concentration Pathways Scenario 8.5 (RCP8.5), which leads to ~ 940 ppm CO_2 by the end of the century, and a 0.62 m mean sea level rise projected by the IPCC-AR5(49). The historic run has been validated against WTD, soil moisture, evapotranspiration, streamflow and flooding, and total terrestrial water storage (against GRACE) observations (19, 20, 28, 46).

We calculate waterlogging and drought stress SEVs as discussed above and use the difference between the historical and future run to identify areas currently covered by forest and not exposed to double stress but will be exposed to double stress in the future. To identify only those forests exposed to the most stressful conditions, we use only combinations of drought and waterlogging SEVs associated with savanna dominance greater than 62.5% (oranges and red bins in Fig. 2).

8. Upscaling

Because most of our datasets are at different spatial resolutions, we adopt the following upscaling procedures. First, we upscale the MAPBIOMAS and Copernicus products from their original resolutions (30 and 100 m, respectively) to the native MODIS resolution (250 m) using average resampling using the *rasterio* package on land cover data with pixel_value = 1 representing human-influenced pixels and pixel_value = 0 representing natural vegetation. With this methodology, we can assess the percentage of each MODIS pixel that is affected by non-natural cover. We upscale tree cover to the two water table data resolutions using an average algorithm. Because the averaging algorithm in *rasterio* takes the

average of all non-invalid pixels within the larger pixel, we use an 80% valid threshold to avoid small sample sizes inside each larger pixel.

9. Software

All data analyses were performed in Python 3.9.5. Potential analysis was performed in MATLAB R2020a.

References

1. M. Hirota, M. Holmgren, E. H. V. Nes, M. Scheffer, Global Resilience of Tropical Forest and Savanna to Critical Transitions. *Science* **334**, 232–235 (2011).

2. M. Holmgren, M. Hirota, E. H. van Nes, M. Scheffer, Effects of interannual climate variability on tropical tree cover. *Nat. Clim. Change* **3**, 755–758 (2013).

3. A. Staal, S. C. Dekker, C. Xu, E. H. van Nes, Bistability, Spatial Interaction, and the Distribution of Tropical Forests and Savannas. *Ecosystems* **19**, 1080–1091 (2016).

4. E. H. van Nes, M. Hirota, M. Holmgren, M. Scheffer, Tipping points in tropical tree cover: linking theory to data. *Glob. Change Biol.* **20**, 1016–1021 (2014).

5. A. C. Staver, S. Archibald, S. A. Levin, The Global Extent and Determinants of Savanna and Forest as Alternative Biome States. *Science* **334**, 230–232 (2011).

6. L. L. Bourgeau-Chavez, *et al.*, Advances in Amazonian Peatland Discrimination With Multi-Temporal PALSAR Refines Estimates of Peatland Distribution, C Stocks and Deforestation. *Front. Earth Sci.* **9**, 676748 (2021).

7. D. M. Olson, *et al.*, Terrestrial Ecoregions of the World: A New Map of Life on Earth. *BioScience* **51**, 933 (2001).

8. DiMiceli, Charlene, *et al.*, MOD44B MODIS/Terra Vegetation Continuous Fields Yearly L3 Global 250m SIN Grid V006 (2015) https:/doi.org/10.5067/MODIS/MOD44B.006 (November 12, 2021).

9. N. P. Hanan, A. T. Tredennick, L. Prihodko, G. Bucini, J. Dohn, Analysis of stable states in global savannas: is the CART pulling the horse? *Glob. Ecol. Biogeogr.* **23**, 259–263 (2014).

10. N. P. Hanan, A. T. Tredennick, L. Prihodko, G. Bucini, J. Dohn, Analysis of stable states in global savannas - a response to Staver and Hansen: Correspondence. *Glob. Ecol. Biogeogr.* **24**, 988–989 (2015).

11. A. C. Staver, M. C. Hansen, Analysis of stable states in global savannas: is the CART pulling the horse? - a comment: Correspondence. *Glob. Ecol. Biogeogr.* **24**, 985–987 (2015).

12. C. Xu, *et al.*, Remotely sensed canopy height reveals three pantropical ecosystem states. *Ecology* **97**, 2518–2521 (2016).

13. C. M. Souza, *et al.*, Reconstructing Three Decades of Land Use and Land Cover Changes in Brazilian Biomes with Landsat Archive and Earth Engine. *Remote Sens.* **12**, 2735 (2020).

14. M. Buchhorn, *et al.*, Copernicus Global Land Service: Land Cover 100m: collection 3: epoch 2017: Globe (2020) https:/doi.org/10.5281/ZENODO.3518036 (August 26, 2022).

15. V. N. Livina, F. Kwasniok, T. M. Lenton, Potential analysis reveals changing number of climate states during the last 60 kyr. *Clim. Past* **6**, 77–82 (2010).

16. A. Staal, *et al.*, Forest-rainfall cascades buffer against drought across the Amazon. *Nat. Clim. Change* **8**, 539–543 (2018).

17. J. Muñoz Sabater, ERA5-Land monthly averaged data from 1950 to 1980. *Copernic. Clim. Change Serv. C3S Clim. Data Store CDS* **10** (2021).

18. M. Nogueira, Inter-comparison of ERA-5, ERA-interim and GPCP rainfall over the last 40 years: Process-based analysis of systematic and random differences. *J. Hydrol.* **583**, 124632 (2020).

19. G. Miguez-Macho, Y. Fan, The role of groundwater in the Amazon water cycle: 1. Influence on seasonal streamflow, flooding and wetlands. *J. Geophys. Res. Atmospheres* **117** (2012).

20. G. Miguez-Macho, Y. Fan, The role of groundwater in the Amazon water cycle: 2. Influence on seasonal soil moisture and evapotranspiration. *J. Geophys. Res. Atmospheres* **117** (2012).

21. Y. Fan, G. Miguez-Macho, E. G. Jobbágy, R. B. Jackson, C. Otero-Casal, Hydrologic regulation of plant rooting depth. *Proc. Natl. Acad. Sci.* **114**, 10572–10577 (2017).

22. G. Miguez-Macho, Y. Fan, Spatiotemporal origin of soil water taken up by vegetation. *Nature*, 1–5 (2021).

23. Y. Fan, H. Li, G. Miguez-Macho, Global Patterns of Groundwater Table Depth. *Science* **339**, 940–943 (2013).

24. G. Miguez-Macho, Y. Fan, C. P. Weaver, R. Walko, A. Robock, Incorporating water table dynamics in climate modeling: 2. Formulation, validation, and soil moisture simulation. *J. Geophys. Res. Atmospheres* **112**, 2006JD008112 (2007).

25. Y. Fan, G. Miguez-Macho, C. P. Weaver, R. Walko, A. Robock, Incorporating water table dynamics in climate modeling: 1. Water table observations and equilibrium water table simulations: WATER TABLE OBSERVATIONS. *J. Geophys. Res. Atmospheres* **112** (2007).

26. Y. Fan, G. Miguez-Macho, A simple hydrologic framework for simulating wetlands in climate and earth system models. *Clim. Dyn.* **37**, 253–278 (2011).

27. Y. Fan, G. Miguez-Macho, Potential groundwater contribution to Amazon evapotranspiration. *Hydrol. Earth Syst. Sci.* **14**, 2039–2056 (2010).

28. Y. N. Pokhrel, Y. Fan, G. Miguez-Macho, P. J.-F. Yeh, S.-C. Han, The role of groundwater in the Amazon water cycle: 3. Influence on terrestrial water storage computations and comparison with GRACE: AMAZON GROUNDWATER AND TWS VARIATION. *J. Geophys. Res. Atmospheres* **118**, 3233–3244 (2013).

29. D. Selhorst, I. F. Brown, LBA-ECO LC-02 Groundwater Levels, Catuaba Experimental Farm, Acre, Brazil: 1999-2004 (2012) https:/doi.org/10.3334/ORNLDAAC/1062.

30. N. R. Do Nascimento, *et al.*, Podzolization as a deferralitization process: dynamics and chemistry of ground and surface waters in an Acrisol–Podzol sequence of the upper Amazon Basin. *Eur. J. Soil Sci.* **59**, 911–924 (2008).

31. A. S. Bastos, Estudo do Comportamento do Fluxo de Água Na Zona Saturada da Reserva Biológica do Cuieiras, Amazônia Central. Thesis. *Inst. Nac. Pesqui. Amaz.* (2019).

32. J. Grogan, J. Galvão, Physiographic and floristic gradients across topography in transitional seasonally dry evergreen forests of southeast Pará, Brazil. *Acta Amaz.* **36**, 483–496 (2006).

33. L. S. Borma, *et al.*, Atmosphere and hydrological controls of the evapotranspiration over a floodplain forest in the Bananal Island region, Amazonia. *J. Geophys. Res. Biogeosciences* **114** (2009).

34. S. Swenson, J. Wahr, P. C. D. Milly, Estimated accuracies of regional water storage variations inferred from the Gravity Recovery and Climate Experiment (GRACE). *Water Resour. Res.* **39** (2003).

35. F. W. Landerer, S. C. Swenson, Accuracy of scaled GRACE terrestrial water storage estimates. *Water Resour. Res.* **48** (2012).

36. NASA/JPL, CSR TELLUS GRACE Level-3 Monthly Land Water-Equivalent-Thickness Surface Mass Anomaly Release 6.0 version 04 in netCDF/ASCII/GeoTIFF Formats (2021) https:/doi.org/10.5067/TELND-3AC64 (February 14, 2022).

37. R. de O. Xavier, M. B. Leite, K. Dexter, D. M. da Silva Matos, Differential effects of soil waterlogging on herbaceous and woody plant communities in a Neotropical savanna. *Oecologia* **190**, 471–483 (2019).

38. M. B. Leite, R. O. Xavier, P. T. S. Oliveira, F. K. G. Silva, D. M. Silva Matos, Groundwater depth as a constraint on the woody cover in a Neotropical Savanna. *Plant Soil* **426**, 1–15 (2018).

39. R. Villalobos-Vega, *et al.*, Do groundwater dynamics drive spatial patterns of tree density and diversity in Neotropical savannas? *J. Veg. Sci.* **25**, 1465–1473 (2014).

40. J. Silvertown, M. E. Dodd, D. J. G. Gowing, J. O. Mountford, Hydrologically defined niches reveal a basis for species richness in plant communities. *Nature* **400**, 61–63 (1999).

41. T. M. Cover, *Elements of information theory* (John Wiley & Sons, 1999).

42. X. Feng, A. Porporato, I. Rodriguez-Iturbe, Changes in rainfall seasonality in the tropics. *Nat. Clim. Change* **3**, 811–815 (2013).

43. L. E. O. Aragão, *et al.*, Spatial patterns and fire response of recent Amazonian droughts. *Geophys. Res. Lett.* **34** (2007).

44. A. C. Staver, W. J. Bond, W. D. Stock, S. J. van Rensburg, M. S. Waldram, Browsing and fire interact to suppress tree density in an African savanna. *Ecol. Appl.* **19**, 1909–1919 (2009).

45. J. Lloyd, *et al.*, Edaphic, structural and physiological contrasts across Amazon Basin forest–savanna ecotones suggest a role for potassium as a key modulator of tropical woody vegetation structure and function. *Biogeosciences* **12**, 6529–6571 (2015).

46. Y. N. Pokhrel, Y. Fan, G. Miguez-Macho, Potential hydrologic changes in the Amazon by the end of the 21st century and the groundwater buffer. *Environ. Res. Lett.* **9**, 084004 (2014).

47. D. Yamazaki, S. Kanae, H. Kim, T. Oki, A physically based description of floodplain inundation dynamics in a global river routing model: FLOODPLAIN INUNDATION DYNAMICS. *Water Resour. Res.* **47** (2011).

48. N. Gedney, P. M. Cox, H. Douville, J. Polcher, P. J. Valdes, Characterizing GCM Land Surface Schemes to Understand Their Responses to Climate Change. *J. Clim.* **13**, 3066–3079 (2000).

49. Intergovernmental Panel on Climate Change, Ed., "Sea Level Change" in *Climate Change 2013 – The Physical Science Basis*, 1st Ed., (Cambridge University Press, 2014), pp. 1137–1216.